First-principles studies of the stability of Zintl ions in alkali-tin alloys: II. Liquid alloys

First-principles studies of the stability of Zintl ions in alkali–tin alloys: II. Liquid alloys

O Genser and J Hafner

Institut für Materialphysik and Centre for Computational Materials Science, Universität Wien, Sensengasse 8/12, A-1090 Wien, Austria

Abstract

Following our preceding work on the structure and electronic properties of crystalline Zintl phases in alkali–tin systems, we have studied the structural, dynamic and electronic properties of these alloys in the molten state using *ab initio* local density functional molecular dynamics. Extended simulations (up to 124 atoms per cell, simulation times of up to 60 ps) have been performed for K–Sn, in which, according to the results for the crystalline compounds, the tetrahedral Sn_4 polyanions can be expected to be most stable. Simulations at the experimental density and starting from configurations with no polyanions at all, but allowing for sufficient time for equilibration, lead to excellent agreement with the structure factor and radial distribution function measured by means of neutron diffraction. The analysis of the instantaneous multi-atom configurations leads to the conclusion that at least a certain fraction of the Sn atoms form polyanionic clusters. The existence of such clusters is also supported by the calculation of the electronic and vibrational spectra; the electronic structure in particular shows the signatures of tetrahedral polyanions. The precise percentage of Sn atoms forming polyanions depends, however, on density and on the ability of the system to simultaneously accommodate all An atoms in electronically saturated clusters. At a slightly higher density we find that a 64-atom ensemble condenses to a 'plastic' or 'rotor' phase in which almost all Sn atoms are arranged in tetrahedral polyanions performing only librational motions, whereas the K atoms continue to show liquid-like behaviour. Simulations for liquid Na–Sn and Li–Sn show a less complex behaviour: in the melt the Sn atoms form an entangled three-dimensional network instead of isolated polyanions. Again the calculated structure factors are in good agreement with diffraction measurements. The analysis of the vibrational and electronic spectra confirms the breakdown of polyanionic ordering. The trend in the series K, Na, Li–Sn is attributed to the decreasing size of the alkali atoms which leads to a less efficient screening of the polyanions by a surrounding shell of alkali atoms. The Zintl picture for the chemical bonding is supported insofar as we find that the electronic and chemical bonding properties are dominated by the strong attractive potential of the polyvalent Sn atoms resulting in the formation of at least partially covalent Sn–Sn bonds.

(Some figures in this article are in colour only in the electronic version; see www.iop.org)

1. Introduction

In the preceding paper of this series devoted to the investigation of polyanionic bonding in alkali–group-IV alloys [1] (hereafter referred to as I) we have presented a comprehensive local density functional (LDF) study of the crystal structure, phase stability, electronic structure and chemical bonding properties of equiatomic (Li/Na/K)–Sn alloys, illustrating the transition from essentially ionic (i.e. saltlike) bonding to polyanionic bonding with strong covalent bonds within the polyanionic clusters with increasing size of the alkali atom. Our results serve to confirm and to reinterpret the Zintl principle for the formation of polyanions: in the original form, the Zintl argument requires the transfer of all valence electrons from the alkali atom to its more electronegative partner, so the tetrahedral Sn_4^{4-} polyanions found in crystalline KSn and NaSn would indeed be isoelectronic and isomorphic to the P_4 molecule. Our LDF studies have demonstrated that spatial charge transfer is not the main point. The decisive feature of a polyanionic compound is that all occupied valence states are determined by the strong attractive electron–ion potential of the polyvalent element and may be described in terms of linear combinations of its atomic eigenstates. For KSn and NaSn alloys this is beautifully illustrated by the structure of the valence band, which may be indexed in terms of the irreducible representations of the tetrahedron group.

The investigation of crystalline Zintl alloys already has a long history, starting with the seminal work of Zintl and co-workers in the 1930s [2]. The recent revival of interest in this topic stems from the fact that investigations of the crystalline compounds at elevated temperatures and of the molten alloys have demonstrated the exceptional stability of certain polyanionic units, in particular of the tetrahedral polyanions formed in alkali–group-IV alloys. High-temperature phase transitions to plastic (rotor) phases with diffusive disorder of the alkali ions and rotational motion of the polyanions have been detected in NaSn and CsPb [3, 4]. Diffraction experiments on molten alkali–Sn and alkali–Pb alloys have demonstrated the existence of a pronounced chemical and topological short-range order (CSRO and TSRO), which has been interpreted as evidence for the at least partial survival of the polyanions in the liquid phase [5–13]. This interpretation is supported by the analysis of the thermodynamic and electronic transport properties; see I for a more detailed discussion and references. Quench-condensation experiments [14–16] demonstrate the existence of similar, even more pronounced anomalies in the electronic properties of amorphous NaSn and KSn, linked to a strong CSRO and TSRO.

The problem is that diffraction experiments, even if they succeed in resolving the partial structure factors and pair correlation functions of the alloy, provide only a one-dimensional projection of the three-dimensional structure. Attempts have been made to reconstruct the three-dimensional atomic configurations from the diffraction data using reverse Monte Carlo (RMC) simulations, finding only little evidence for the existence of polyanions [17, 18]. After all, this is not surprising since by construction RMC calculations tend to produce the most disordered structure compatible with the diffraction data.

More significant is that even the most sophisticated *ab initio* LDF molecular dynamics (MD) simulations [19–23, 25] suggest the existence of a variety of local conformations of the group-IV atoms, linked together to form an extended network, rather than the existence of a substantial fraction of isolated tetrahedra as inferred on the basis of the diffraction data and the sharp anomalies observed in so many different physical properties. There are several difficulties with the *ab initio* MD simulations presented so far. The first is our inability to establish systematic trends: Li–Si alloys [21] do not form tetrahedral polyanions even in the crystalline state; in Na–Sn alloys [20, 23–25] the crystalline polyanionic compound has marginal stability—it coexists with several near-octet compounds with saltlike structures [26].

It is therefore not surprising that the MD simulations failed to predict polyanion formation in these materials [20, 21, 23–25]. Only for molten K–Si [19] and Cs–Pb [22] should polyanion formation have been expected, given the dominant role of the crystalline polyanionic compound in the phase diagram. The second difficulty concerns the uncertainty of the density of the polyanionic melt. In the crystalline phase, the polyanionic compounds are characterized by large negative volumes of formation ($\Delta\Omega = -17.2\%$ for NaSn, $\Delta\Omega = -28.3\%$ for KSn), but the DFT calculations suggest that the simple ionic structures would show even larger contractions on alloying (cf. the discussion in I). The *ab initio* MD simulations have been performed either at the experimental density of the alloy (which tends to be rather inaccurate, because the data are inferred from the low-R part of the measured correlation functions rather than determined by densitometric experiments) [21, 22] or even at the density of the solid intermetallic compound (which probably represents a rather gross overestimate of the negative excess volume) [20, 23]. The third difficulty consists certainly in the restricted system size and the short duration of the computer experiments, which make it very difficult to obtain an extended sampling of well-equilibrated configurations.

The priorities in the present work are to resolve these difficulties: by performing *ab initio* MD simulations on the series of molten Li–Sn, Na–Sn and K–Sn alloys, we succeed in establishing clear structural trends. By optimizing the density of the molten alloy in a series of constant-volume simulations, we uniquely determine the equilibrium structure, and we study the influence of varying density on the stability of the polyanionic clusters. Our simulations are also extended over time spans rather unusual in *ab initio* MD simulations, and are performed for ensembles about twice as large as in most previous *ab initio* MD studies of liquid alloys. This allows for a thorough equilibration of the system and for an extended sampling of configuration space.

Our paper is organized as follows. In section 2 we briefly recapitulate the methodological aspects, concentrating on those details that are unique for *ab initio* DFT studies of liquid materials. Sections 3 to 5 present our results for the structural, dynamic and electronic properties of molten K–Sn, Na–Sn and Li–Sn. The systematic trends in the liquid and electronic properties resulting from these studies are discussed in section 6 and we conclude in section 7.

2. Methodology

Our calculations are based on local density functional theory as implemented in the Vienna *ab initio* simulation package (VASP) [27, 28]. VASP works in a plane-wave basis and uses ultrasoft pseudopotentials for describing the electron–ion interaction. For all technical details we refer the reader to the references given in I, where we have also presented all the information relevant to the choice of the pseudopotentials.

VASP performs an analytic calculation of the Hellmann–Feynman forces acting on the atoms and of the stresses acting on the unit cell. *Ab initio* molecular dynamics (MD) simulations have been performed for a constant-volume ensemble using a Nosé thermostat [29, 30] (see table 1). Since the stresses on the unit cell are known, in principle a constant-temperature constant-pressure simulation based on a Nosé–Andersen or Parrinello–Rahman–Nosé Hamiltonian [31, 32] or a constant-stress simulation using a Ray–Rahman–Nosé Hamiltonian [33] could have been performed. However, previous experience [34] tells us that fluctuations in the internal strains and stresses tend to be large, especially in ensembles as small as those that are accessible to *ab initio* simulations. Such fluctuations would tend to obscure the structural correlations, so constant-volume simulations are preferable. It is imperative, however, to determine the zero-pressure volume as precisely as possible. The crystalline phases are characterized by large negative excess volumes varying considerably

Table 1. Parameters for *ab initio* molecular dynamics simulations of molten alkali–tin alloys.

	KSn	NaSn	LiSn
Number of atoms	64/96/124	124	124
Mass of alkali atom (au)	39.10	22.99	6.94
Mass of Sn atom (au)	118.71	118.71	118.71
Atomic volume (Å^3)	38.44/43.8	28.60	22.13
Number density (Å^{-3})	0.026/0.023	0.035	0.045
Temperature (K)	1150	851	765
Nosé mass (au)	2.0	2.0	2.0
Time steps (fs)	3	3	3
Duration of simulation (ps)	$\leqslant 60.0$	20.0	15.0

with the assumed crystal structure (note that the alloying contraction tends to be weaker in the polyanionic than in simpler ionic structures; cf. table 7 in I). In the present work the equilibrium volume of the liquid alloys has been derived from a series of short constant-volume simulations at different densities during which the internal pressure was monitored. Extended MD simulations were performed at the zero-pressure density derived from these exploratory runs, carefully monitoring the pressure fluctuations. However, it has to be admitted that due to the dependence of the excess volume on the nature and the degree of local ordering, such a procedure cannot yield more than a first-order estimate. Therefore we have also investigated the influence of variations in the atomic volume of the liquid structure and electronic properties.

Integration of the equations of motion in the extended phase space of Nosé dynamics was performed using a Verlet algorithm with a time step of $\Delta t = 3$ fs. Note that since we calculate the exact LDF ground state after any ionic move, the system remains always exactly on the Born–Oppenheimer surface and the time step is determined by the ionic dynamics alone. Our results demonstrate that even for very long MD runs (up to 60 ps), the drift in the total free energy is negligible. Hence the use of this relatively large time increment is justified. The 'mass' of the Nosé thermostat is chosen such that the characteristic frequency of the thermostat falls within the range of the vibrational eigenfrequencies of the system. In this way an efficient equilibration can be achieved [29, 30].

The exact number of particles turned out to have a rather pronounced influence on the results of the simulations. All MD runs have been started with the atoms distributed over the sites of a simple cubic lattice, using a 4^3 supercell for the smallest 64-atom ensemble and a 5^3 supercell with a central vacancy for the largest ensemble. For KSn we have in addition considered an ensemble of intermediate size with 96 atoms. Perfect saltlike chemical order on the simple cubic lattice (each atom having six nearest neighbours of the other kind) was assumed for the initial structure. With this starting configuration, any similarity of the local order in the molten alkali–tin alloy with the structures of the crystalline compounds is certainly not the consequence of the choice of the initial structure. On the other hand, it has to be expected that the formation of a high degree of polyanionic order will require extended equilibration times. To accelerate melting, the MD simulation was started at a high temperature ($T = 1500$ K for LiSn and NaSn, $T = 1550$ K for KSn) and equilibrated for 1000 time steps ($\equiv 3$ ps). After this initial phase, the temperature was lowered to a value close to the melting point of the crystalline compound and continued at least for 12 ps. For some models, the simulations have been extended to about 60 ps to ensure complete equilibration with respect to the chemical and topological short- and medium-range order.

3. Molten K–Sn alloys

The MD simulations of equiatomic KSn alloys showed a strong dependence of the results on the density, the number of atoms in the ensemble, the chosen initial configuration and the duration of the simulation. To bring some systematics into this variety, we begin with a description of the simulation history.

3.1. Simulation history

Our MD simulations for liquid K–Sn alloys were started with a 64-atom ensemble and the initial configuration described above. A series of short MD runs led to a zero-pressure volume of $\Omega = 38.4$ Å^3/atom at a temperature of $T = 1150$ K. This corresponds to an excess volume of $\Delta\Omega = -21.3\%$, i.e. the volume contraction on alloying is considerably smaller in the liquid than in the crystalline state where we had found an excess volume of about -32.5%. A long MD run was performed at this constant volume. Convergence was found to be quite slow, but after about 30 ps the system assumed a well-ordered polyanionic structure and showed a very deep pseudogap in the electronic density of states at the Fermi level. As the simulation was extended up to 60 ps, the pseudogap continued to deepen, although the partial structure factors remained essentially unchanged. The calculated neutron-weighted structure factor showed excellent agreement with the inelastic neutron diffraction data.

To improve the statistics of the computer experiment, the MD simulations were repeated for a 124-atom ensemble, with an almost identical starting configuration. Surprisingly, the characteristic polyanionic local order was very slow to develop: after about 30 ps the K–K and K–Sn partial pair correlation functions showed good agreement with those calculated for the 64-atom ensemble, but considerable differences were found in the Sn–Sn correlation functions. The much lower intensity of the prepeak in the Sn–Sn and the concentration–concentration fluctuation structure factors, and the analysis of the angular correlations between the Sn–Sn bonds also indicated a much lower degree of local order, impairing to some degree the agreement with experiment. The question was hence how such strong size effects could arise.

Examination of the atomic dynamics showed that the development of polyanionic order in the small 64-atom ensemble was paralleled by a slowing down of the atomic dynamics, which affected K and Sn atoms in very different ways: whereas the K dynamics remained predominantly diffusive, the diffusive motion of the Sn atoms came to an almost complete arrest. A detailed analysis of the three-dimensional arrangement of the atoms demonstrated that the majority of the Sn atoms formed more or less perfect Sn$_4$ tetrahedra; a characteristic instantaneous configuration is shown in figure 1. These tetrahedral clusters performed vibrational and librational movements, but their centre of gravity fluctuated around well-defined equilibrium sites. This is demonstrated in figure 2 which shows the trajectories of the centre of gravity of the Sn$_4$ tetrahedra during a time span of 6 ps, projected onto the xy-, yz- and zx-planes. We find that the tetrahedra form a well-ordered three-dimensional arrangement which is similar to that in the NaPb-type crystal structure (cf. figure 1 in I). The possibility of crystallization into the NaPb structure however is excluded, because the cubic MD cell is incompatible with the orthorhombic Na–Pb cell. Occasionally, the trajectories are interrupted and continued somewhere else in the cell. This indicates that due to a large displacement amplitude, a close contact with atoms in a neighbouring tetrahedron is formed and the atoms regroup in a different way. However, such configurations are seen to be extremely short lived and the atoms always return to the same polyanionic cluster. Altogether this state is best characterized as being very similar to the 'plastic' or 'soft' phase described by Price
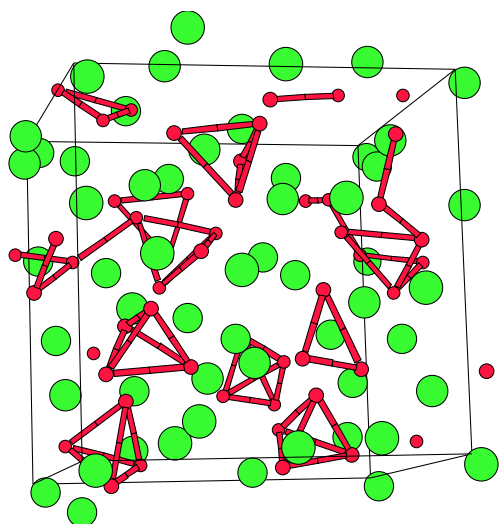
Figure 1. The instantaneous configuration of the 64-atom ensemble representing liquid KSn at a density of $n = 0.026$ Å^{-3}. Large grey circles represent K atoms, smaller dark circles Sn atoms. Sn–Sn bonds shorter than 3 Å are drawn as solid bars. The lines represent the boundaries of the MD box. Note that almost all Sn atoms belong to one of the Sn$_4$ tetrahedra. See the text.
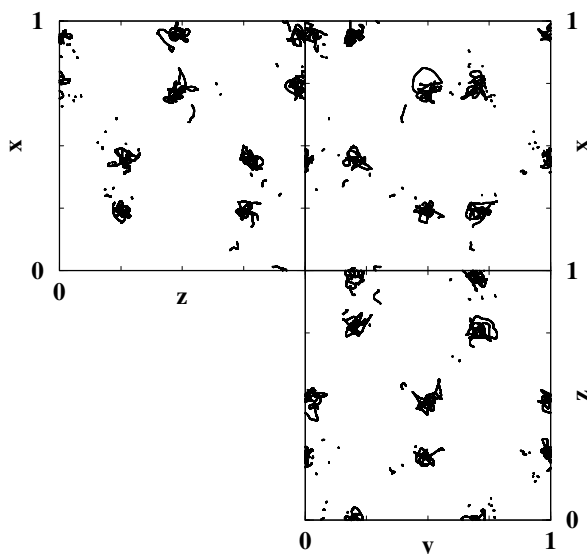
KSn 64

Figure 2. Trajectories of the centre of gravity of the tetrahedral Sn$_4$ polyanions formed in the 64-atom ensemble of KSn at $n = 0.026$ Å^{-3}, projected on the three coordinate planes. The trajectories represent the dynamical evolution of the system during a time interval of 7.5 ps. See the text.

et al [35–37]. This phase was found during a two-stage melting process of the crystalline intermetallic compounds NaSn and CsPb whose structure is isotypic to that of KSn.

On the other hand, both species were found to diffuse rather fast in the larger 124-atom ensemble. Sn$_4$ clusters were continuously formed, but broke apart after a rather short time interval. At a given moment, only a small percentage of the Sn atoms could be associated with more or less deformed Sn$_4$ tetrahedra. Figure 3 shows a characteristic instantaneous configuration of the 124-atom ensemble, figure 4 the projected trajectories of the centre of
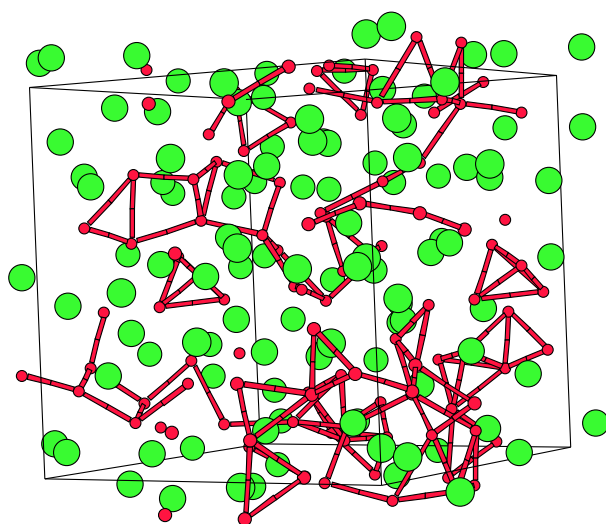
Figure 3. The instantaneous configuration of the 124-atom ensemble representing liquid KSn at a density of $n = 0.026$ Å^{-3}. See figure 1.
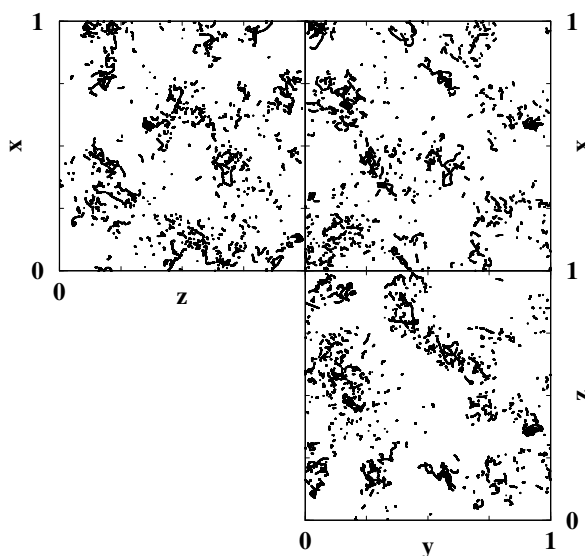
KSn 124

Figure 4. Trajectories of the centre of gravity of tetrahedral Sn$_4$ clusters formed in the 124-atom ensemble of KSn at $n = 0.026$ Å^{-3}; cf. figure 2.

gravity of the Sn$_4$ tetrahedra (a 'tetrahedron' being defined as any configuration of an atom and its three nearest neighbours). It is evident that the lifetime of most of these clusters is extremely short, although some of them survive for larger time intervals.

Another observation was that although the internal pressure showed rather large fluctuations, in particular in the small ensemble, the results for the large ensemble demonstrated that the gradual development of polyanionic order led also to a slow increase of the internal pressure. This agrees with our results for the crystalline phases where we had found that a hypothetical K–Sn phase with more saltlike order had an even larger negative excess volume

than the polyanionic phase. Since in our starting configuration each atom is surrounded by atoms of the second species only, it is not surprising that our short MD runs used for calibrating the equilibrium volume led to a density that was too large. In view of the difficulties associated with constant-pressure *ab initio* MD simulation, we decided to repeat both runs at the experimental atomic volume. Experimentally, the number density of the molten alloy has been estimated from the neutron diffraction data (essentially from the slope of the reduced radial distribution function $G(R) = 4\pi Rn(g(R) - 1)$ at small R where $g(R)$ is the total pair correlation function), leading to an atomic volume of $\Omega_L = 42.6$ Å^3 [11] compared to $\Omega_S = 37.84$ Å^3 for the crystalline compound at room temperature [39]. However, it is certainly legitimate to emphasize that the experimental densities determined in that way are subject to a rather large uncertainty.

The simulations for the smaller ensemble showed a relatively strong dependence on the starting configuration: if the simulation was started from the relaxed dense structure rescaled to the larger volume, the system remained in the 'plastic' phase with frozen polyanionic configurations of the Sn atoms. If the simulations were restarted from scratch, polyanionic order developed more slowly, but after about 40 ps the system equilibrated again in a state with a large degree of polyanionic order. Although the pair correlation functions and partial static structure factors were found to be almost identical to the former high-density results, the analysis of the three-dimensional atomic arrangements and of the atomic dynamics demonstrated that at this lower density the mobility of the Sn_4 tetrahedra was high enough to allow from time to time close contacts between Sn atoms belonging to different tetrahedra which in most cases led to the formation of short-lived large clusters disintegrating quickly into new tetrahedral units.

The simulations for the large 124-atom ensemble also showed only a relatively modest density dependence. The most remarkable change is a slight sharpening of the first peak in the Sn–Sn and density–density structure factors, indicating a somewhat higher degree of local order. However, the difference between the results obtained with the large and small ensembles remains too large to be explained in terms of a simple size effect. At this stage it is important to stress a difference between the 64-atom and 124-atom ensembles which could eventually be significant: in the smaller ensemble, the 32 Sn atoms can form just eight Sn_4 tetrahedra; in the larger ensemble, out of the 62 Sn atoms, fifteen Sn_4 tetrahedra can be formed, but two Sn atoms necessarily remain unbound. The analysis of the time development of the ensemble suggests that these unbound Sn ions represent a rather aggressive chemical species: they are highly mobile and each time they approach an Sn_4 tetrahedron, they tend to attach to this cluster. The stability of these Sn_5 (or even Sn_6) clusters is considerably lower than that of the Sn_4 polyanions with saturated chemical bonds. Consequently they disintegrate rather quickly into smaller Sn_3 or Sn_2 clusters which tend to reform Sn_4 polyanions.

To test this scenario, we performed another MD run using a 96-atom ensemble allowing, as for the 64-atom ensemble, all Sn atoms to bind simultaneously in saturated polyanionic clusters. The results confirmed our hypothesis only to a certain extent: due to the larger system size, equilibration took more time, but finally the ensemble equilibrated in a state which produced a prepeak in the measured structure factor which was as intense as that found in the smaller ensemble at the same density. The Sn–Sn pair correlation function was, however, found to be very similar to that calculated for the 124-atom ensemble and the instantaneous configurations (see figure 5) showed only a marginally increased tendency to form polyanionic tetrahedra. The dynamical evolution of these configurations is analysed in figure 6 where again the trajectories of the centres of the polyhedra are displayed. We find some rather long trajectories indicating a slightly increased stability of the polyanions compared to the 124-atom ensemble.
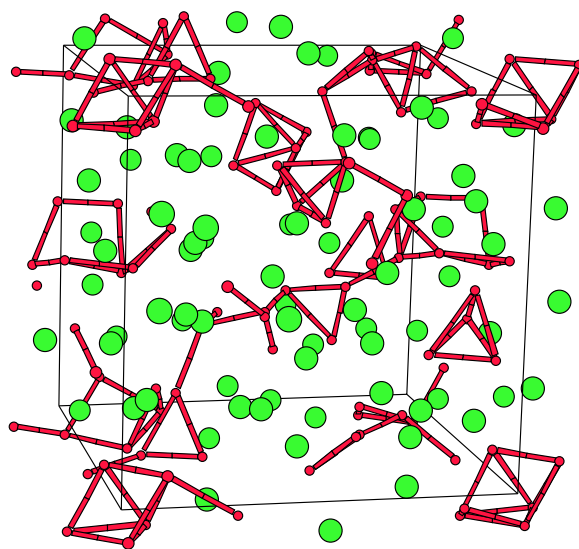
Figure 5. The instantaneous configuration of the 96-atom ensemble representing liquid KSn at a density of $n = 0.023$ Å^{-3}. See figure 1 and the text.

KSn 96

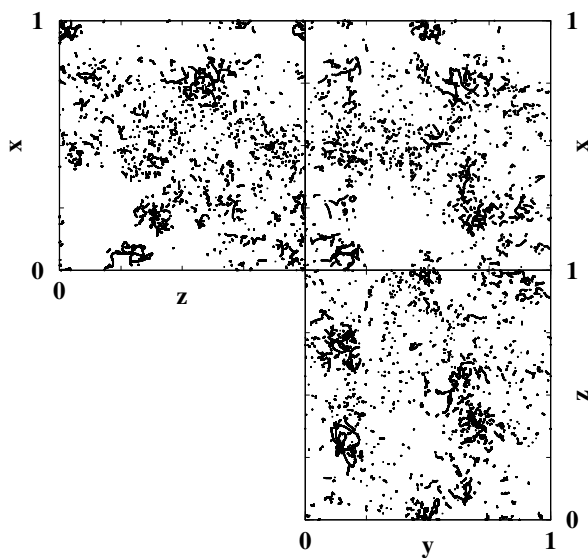**Figure 6.** Trajectories of the centre of gravity of tetrahedral Sn$_4$ clusters formed in the 96-atom ensemble at a density of $n = 0.023$ Å^{-3}. See figure 2 and the text.

To complete the investigations, we have monitored the time evolution of the pressure in the different MD runs. In the small high-density ensemble we find, after an initial increase, that with increasing polyanionic order the internal pressure decreases again, fluctuating around zero in a well-equilibrated state. In the less ordered 124-atom ensemble, the internal pressure remained positive, fluctuating around a value of about 4 kbar. The simulations at

the experimental density produced a small negative pressure of about 4 kbar, indicating that our LDA-based simulations lead to too high an equilibrium density. However, the estimated internal pressure is of the same order of magnitude as the pressure fluctuation in our constant-volume ensemble.

A more accurate density could probably be achieved using gradient corrections to the exchange–correlation functional. For two reasons we decided not to repeat the costly simulations in the GGA:

 (i) As discussed already in I, although the GGA improves agreement with experiment for the alkali metals, it overshoots for the heavy polyvalent elements such as Sn.
 (ii) Numerous studies have shown that at fixed volume, LDA and GGA lead to identical structural predictions (see, e.g., references [54, 55]).

In the following we discuss in detail the atomic structure and dynamics and the electronic properties of the different ensembles representing the molten alloy. The interesting result is that the differences in the local order lead only to rather modest differences in the pair correlation functions and partial structure factors (and hence are hard to recognize in any diffraction experiment), but that striking differences exist in the atomic single-particle dynamics and in the electronic spectra.

3.2. Atomic structure

3.2.1. Pair correlation functions. Figure 7 presents the results for the partial pair correlation functions obtained using both the large (124-atom) and the small (64-atom) ensembles at a density of $n = 0.026$ Å^{-3} estimated from a series of short MD runs with the small ensemble. Both ensembles have been equilibrated over about 60 ps; the correlation functions have each been calculated as a coarse-grained average over the last 18 ps of each run (most other data presented below refer to the same time window of the simulations). We show both the component-related (K–K, K–Sn and Sn–Sn) correlation functions and the density and concentration correlation functions introduced by Bhatia and Thornton [40]. The most characteristic feature is the sharp first peak in the Sn–Sn correlation function and the broad first maximum of the K–K correlation function. Partial coordination numbers can be obtained by integrating over the first peak in the radial distribution functions

$$\text{RDF}_{ij}(R) = 4\pi (n_i n_j)^{1/2} R^2 g_{ij}(R)$$

(with n_i the partial number density), but the procedure is not unique: integration up to the first minimum in $g_{ij}(R)$ considerably overestimates the coordination number, whereas the result of an integration up to the first maximum, multiplied by 2 (i.e. integration over the symmetric part of the first peak) yields realistic numbers which turn out to be very close to those in the crystalline phase (see table 2).

Correlations beyond the nearest-neighbour shell are surprisingly weak, but definitely not hard-sphere-like: for the K–K and K–Sn correlation functions, the ratio of the second- and first-peak positions is $R_2/R_1 \simeq 1.6$ to 1.7; for the Sn–Sn correlation functions the ratio is $R_2/R_1 \simeq 2.2$. Both values differ significantly from the value $R_2/R_1 \simeq 1.86$ characteristic for hard-sphere fluids. The existence of a strong chemical and topological short-range order (CSRO and TSRO) is also confirmed by the Bhatia–Thornton correlation functions: for the density–density correlation we find $R_2/R_1 \simeq 1.62$; hence the packing of the second shell of neighbours around a central cluster cannot be interpreted in terms of an arrangement of hard or soft spheres only. The concentration–concentration correlation function

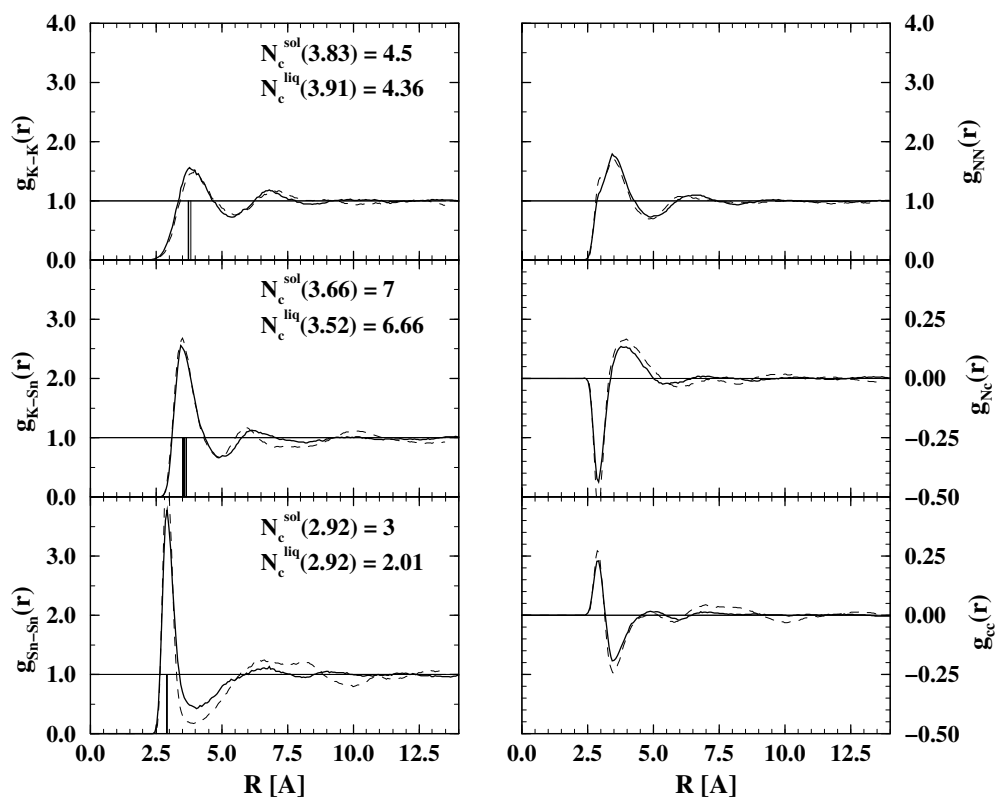$$g_{cc}(R) \simeq (g_{\text{K–K}}(R) + g_{\text{Sn–Sn}}(R) - 2g_{\text{K–Sn}}(R))$$

Figure 7. Partial component-related pair correlation functions $g_{K-K}(R)$, $g_{K-Sn}(R)$, $g_{Sn-Sn}(R)$ and density and concentration correlation functions $g_{NN}(R)$, $g_{Nc}(R)$ and $g_{cc}(R)$, for liquid K–Sn at $T = 1150$ K and $n = 0.026$ Å^{-3}. Full lines: results calculated for the 124-atom ensemble; broken lines: results calculated for the 64-atom model. Partial coordination numbers in the large ensemble calculated by integration over the symmetric part of the first peak are given in the individual panels; coordination numbers for all ensembles treated in this study are summarized in table 2. The vertical bars mark the nearest-neighbour distances in crystalline K–Sn.

is characterized by a positive first peak indicating the dominance of short Sn–Sn bonds, followed by a minimum at a slightly larger distance arising from the packing of a second shell of K atoms around a central Sn cluster. The large amplitudes of the density–concentration correlation function g_{Nc} reflect a strong coupling between TSRO and CSRO. However, both density and concentration correlations decay very rapidly with distance—beyond the second-neighbour distance of ∼6.5 Å all correlation effects are extremely weak.

Differences between the large and the small ensembles are rather modest in the K–K and K–Sn correlation functions; significant differences exist only in the Sn–Sn correlation functions where the smaller ensemble leads to a clear separation of the first and second peaks and more pronounced long-range correlations. The more pronounced first peak leads also to a slightly higher Sn–Sn coordination number in the smaller ensemble. However, these changes have only a minor influence on the Bhatia–Thornton correlation functions. This is surprising in view of the quite different behaviour noted above: the dense 64-atom ensemble represents a 'plastic phase' with a high degree of polyanionic order and no diffusive motion of the Sn_4 tetrahedra, the large 124-atom ensemble a liquid state with a much lower fraction of polyanionic clusters.

Table 2. Partial coordination numbers of liquid and crystalline potassium–tin alloys, calculated for different ensembles and densities of $n = 0.026$ Å^{-3} and $n = 0.023$ Å^{-3} (values in parentheses).

	Crystal		Liquid alloy				
	N_{ij}	R_{max}[a] (Å)	N_{at}	N_{ij}	R_{max}[b] (Å)	N_{ij}	R_{max}[c] (Å)
K–K	4.5	3.83	64	4.47	3.98	7.99	5.51
				(4.42)	(4.16)	(9.01)	(5.98)
			96	(3.99)	(4.07)	(8.26)	(5.77)
			124	4.36	3.91	7.70	5.42
				(4.64)	(4.16)	(8.18)	(5.73)
K–Sn	7.0	3.66	64	7.00	3.51	14.17	4.98
				(5.86)	(3.55)	(12.91)	(5.04)
			96	(6.80)	(3.63)	(13.42)	(5.20)
			124	6.66	3.52	13.91	4.96
				(5.36)	(3.54)	(12.43)	(5.05)
Sn–Sn	3.0	2.92	64	2.40	2.93	3.14	3.82
				(2.32)	(2.95)	(3.20)	(4.05)
			96	(2.08)	(2.93)	(3.44)	(3.88)
			124	2.01	2.92	3.58	4.04
				(1.89)	(2.92)	(3.70)	(4.09)

[a] Largest nearest-neighbour distance in the crystal.
[b] Position of the first maximum in the partial pair correlation function.
[c] Position of the first minimum in the partial pair correlation function.

Simulations at a density of $n = 0.023$ Å^{-3} (corresponding to the experimental density at about 1150 K) have been performed for ensembles with 64, 96 and 124 atoms. Figure 8 compares the low- and high-density results for the large ensemble, figure 9 the results for the 64- and 96-atom ensembles at the experimental density. In the pair correlation functions, the density dependence is rather weak: at lower density we find a certain phase shift in the K–K correlations indicating increased K–K distances, whereas the peak positions in g_{K-Sn} and g_{Sn-Sn} are hardly affected (figure 8). More important is the decrease in the height of the first peak in $g_{K-Sn}(R)$, which parallels an increase of the peak height in $g_{Sn-Sn}(R)$. This indicates a slight increase in the degree of CSRO (see also the partial coordination numbers listed in table 2. At this density, simulations for the 64- and 96-atom ensembles lead to almost perfect agreement as regards the Bhatia–Thornton pair correlation functions, but the Sn–Sn correlation function indicates that the local order is only sightly enhanced in the 96-atom compared to the 124-atom ensemble (see figure 9). It is important to emphasize that this comparison is based on very well-equilibrated states reached only after a sufficiently long equilibration time.

The preceding analysis has shown that even quite pronounced changes in the degree of local order are hardly reflected in the pair correlation functions. A conclusive characterization of the local order requires the examination of multi-particle correlations.

3.2.2. Angular correlations. The tetrahedral Sn$_4$ polyanions existing in the crystalline compounds are characterized by 60° angles between all nearest-neighbour bonds. 60° bond angles are quite common in any close-packed configuration; the important points characterizing tetrahedral clusters are that around each site there are only 60° angles and that there are exactly three of them. Hence a bond-angle statistics alone is not sufficient for characterizing
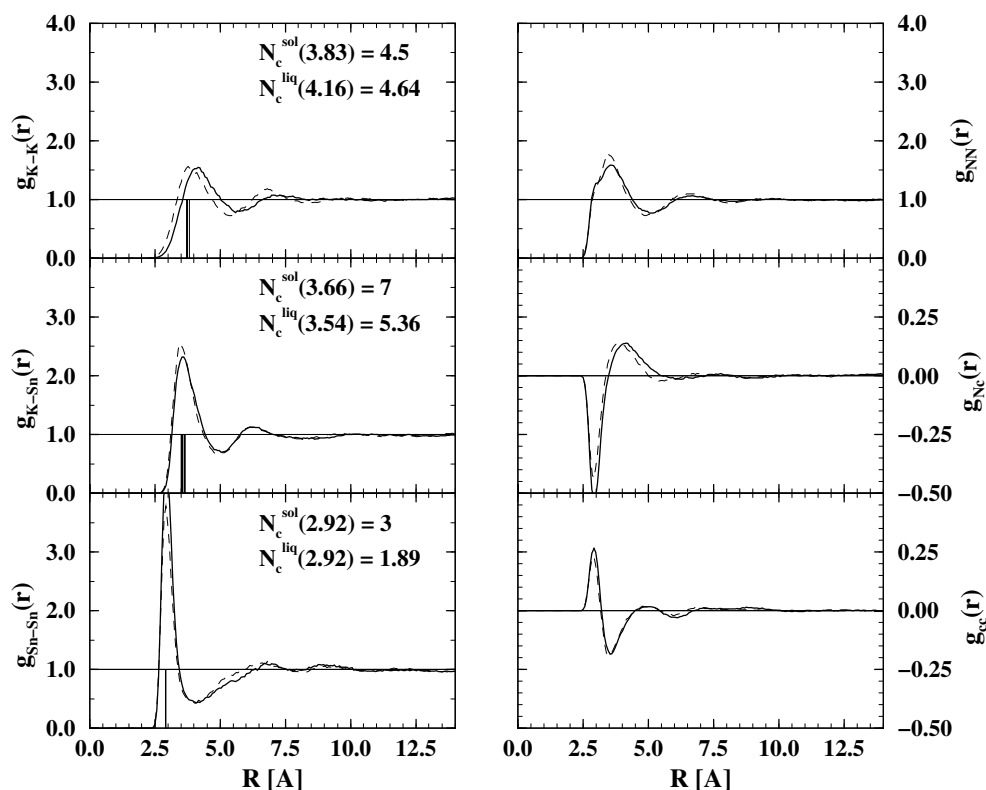
Figure 8. Partial pair correlation functions for liquid K–Sn at $T = 1150$ K, calculated using the 124-atom ensemble at two different densities: solid lines: $n = 0.026$ Å^{-3}; broken lines: $n = 0.023$ Å^{-3}. Coordination numbers given in the individual panels refer to the low-density ensemble.

polytetrahedral ordering. For an analysis of angular correlations in the liquid phase, we proceed in the following way: around each Sn atom, we search for the three shortest Sn–Sn bonds, and we calculate the angles formed between these three bonds. For three typical configurations, the result is plotted in figure 10. For the dense 64-atom ensemble representing the 'plastic phase' characterized by a frozen arrangement of the Sn$_4$ tetrahedra, the bond lengths scatter in a rather narrow range around $R \simeq 3$ Å, as expected from the sharpness of the first peak in the Sn–Sn pair correlation function. The Sn–Sn bond angles are distributed between $50°$ and $70°$, with only a very few much larger angles indicating an instantaneous distortion of a small number of the tetrahedra. This confirms the very high degree of local order in this state—compare also the typical instantaneous configuration shown in figure 1.

An entirely different picture arises from the simulations on the large 96- and 124-atom ensembles (the simulations at the two different densities lead to almost equivalent results): bond lengths and bond angles are distributed over much wider intervals, but it is still possible to identify at least a small fraction of the Sn atoms forming polyanionic clusters of more or less strongly distorted tetrahedral shape. We should also emphasize that formation and disruption of polyanionic bonds is a dynamical process. Whereas the Sn–Sn bonds in complete (and hence electronically saturated) Sn$_4$ units are rather stable and long-lived, the bonds leading to the formation of larger units or of fragments of tetrahedra have only a short lifetime, bond formation and bond breaking occurring on a timescale of a few tenths of a picosecond.
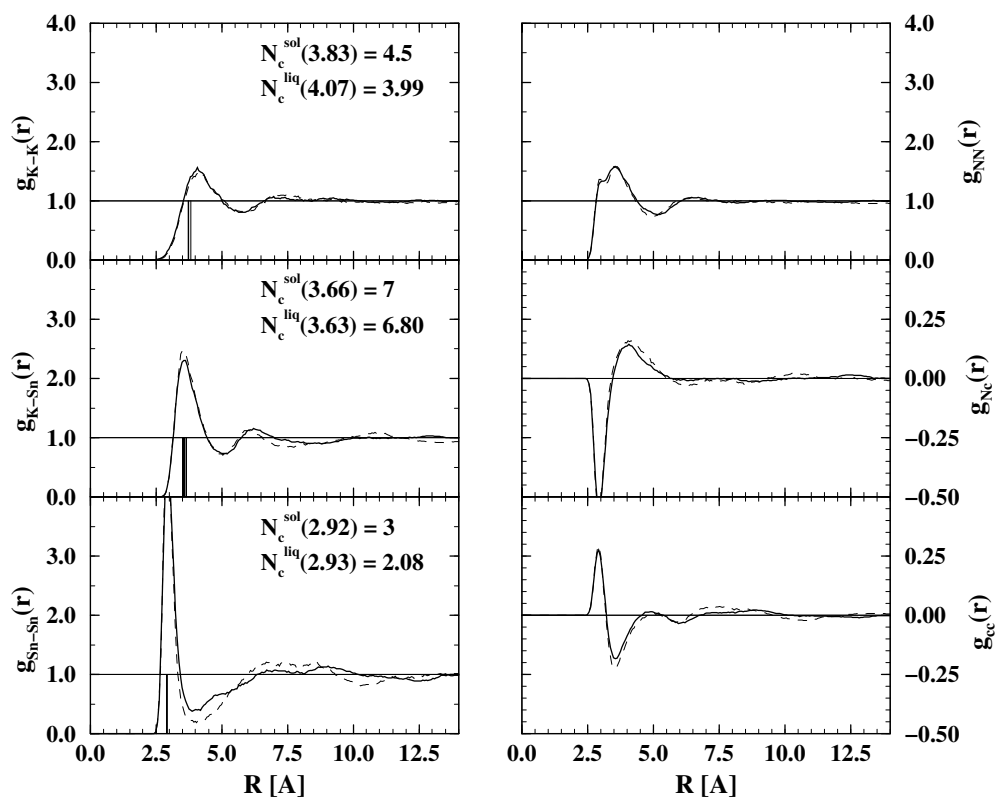
Figure 9. Comparison of the pair correlation functions for liquid K–Sn at $T = 1150$ K and $n = 0.023$ Å^{-3}, calculated using the 96-atom (bold lines) and 64-atom ensembles (broken lines). Coordination numbers given in the individual panels are for the 96-atom ensemble.

3.2.3. Partial structure factors. Figure 11 shows the partial static structure factors calculated for K–Sn at the density $n = 0.026$ Å^{-3} and $T = 1150$ K. Again we have plotted both the component-related and the density–concentration (Bhatia–Thornton) structure factors, and we confront the results obtained for the large and small ensemble. The most characteristic feature of the partial structure factors is the pronounced prepeak in the Sn–Sn and in the concentration-fluctuation structure factors at $q \simeq 1$ Å^{-1} indicating a high degree of chemical short-range order as well as a certain degree of topological ordering. The dominant prepeak in $S_{Sn-Sn}(q)$ arises from strong Sn–Sn correlations over a distance of $R \sim 6$ to 6.5 Å, corresponding to the most frequent distances between separate Sn$_4$ polyanions in the crystalline phase. That a prepeak in $S_{cc}(q)$ occurs at the same momentum transfer indicates that the second-neighbour Sn–Sn distances are determined by K atoms clustering around the Sn polyanions.

In contrast to the pair correlation functions where modest size effects are distributed over a wide range of interatomic distances, in the partial structure factors relatively strong size effects are concentrated in the region of the prepeak. At larger momentum transfers, size effects are essentially below statistical uncertainty. For the larger ensemble, not only is the amplitude of the prepeak reduced in all three partial structure factors, but also we note a shift of the position of the prepeak in $S_{cc}(q)$ to smaller wavenumber, thus indicating a change not only in the intensity, but also in the character of the short-range order.
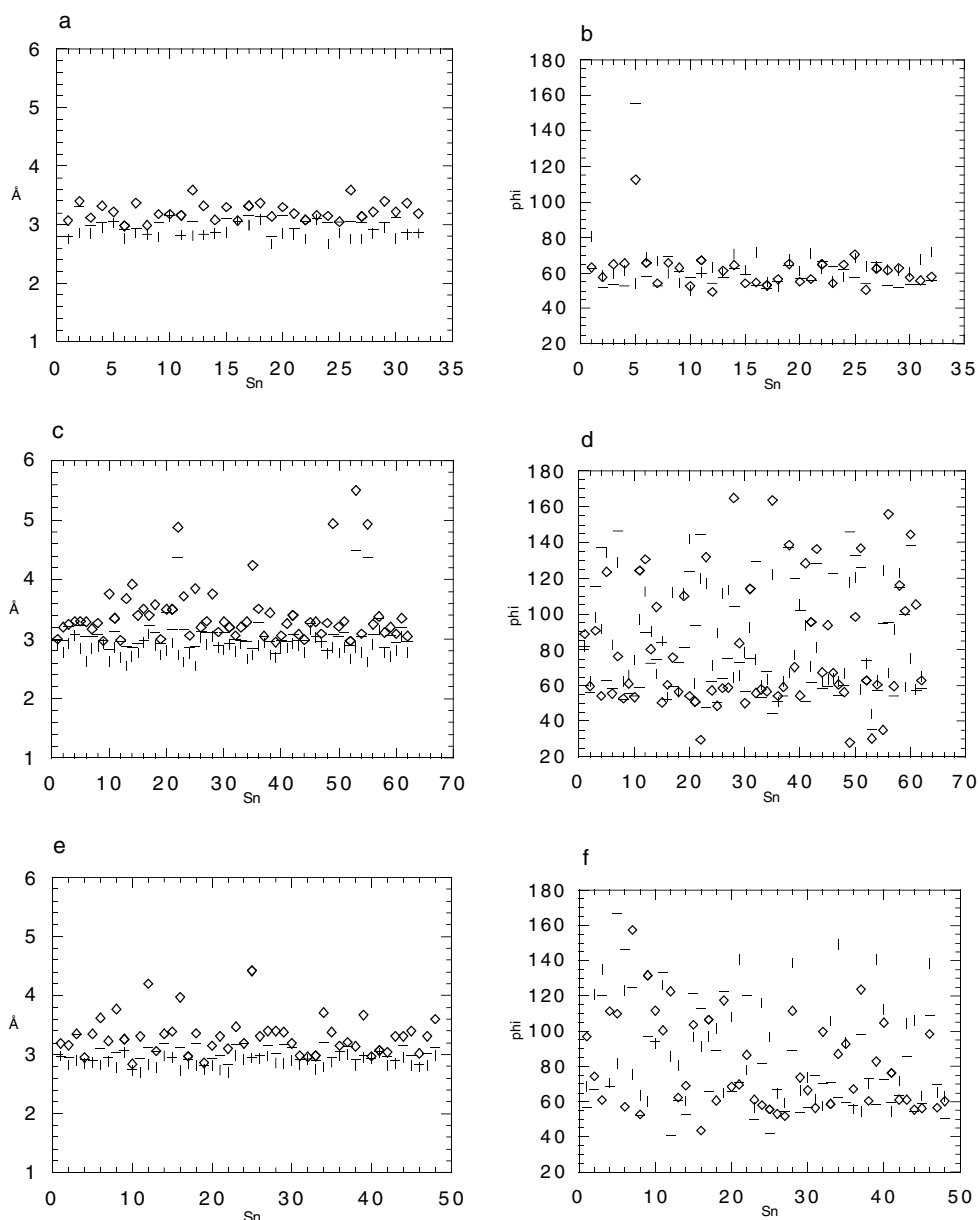
Figure 10. (a) Distribution of the three shortest Sn–Sn bonds around the Sn atoms. (b) Distribution of the Sn–Sn–Sn bond angles as calculated for a typical configuration of the 64-atom ensemble representing liquid K–Sn ($n = 0.026$ Å^{-3}). Parts (c), (d) show the same information for the 124-atom ensemble, parts (e), (f) that for the 96-atom ensembles and $n = 0.023$ Å^{-3}.

Figure 12 compares the partial structure factors calculated for the 64- and 96-atom ensembles at a density of $n = 0.023$ Å^{-3}. In contrast to the result obtained for the 124-atom ensemble, the prepeaks now have essentially the same amplitude as in the more ordered small ensembles. This shows that the pair correlations alone are not sufficient to characterize the degree of local ordering. The tendency to form larger interconnected units in the 96-atom
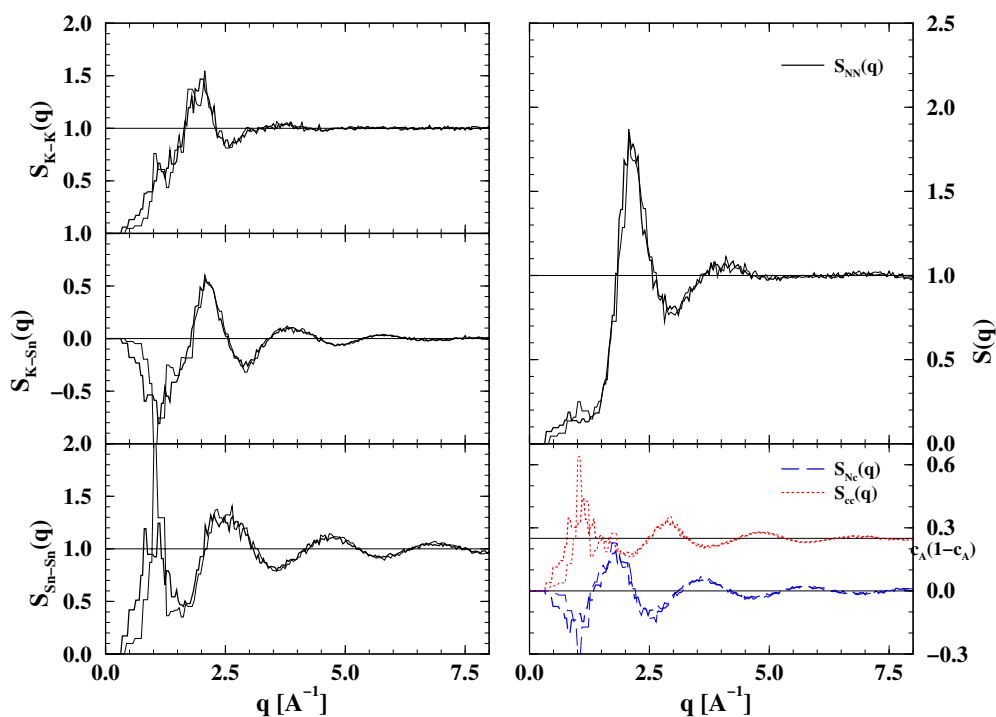
Figure 11. Partial static structure factors for molten K–Sn at $T = 1150$ K and $n = 0.026$ Å^{-3}. Left-hand part: $S_{K-K}(q)$, $S_{K-Sn}(q)$ and $S_{Sn-Sn}(q)$; right-hand part: Bhatia–Thornton partial static structure factors $S_{NN}(q)$, $S_{Nc}(q)$ and $S_{cc}(q)$. Bold lines: results calculated for the 124-atom ensemble; thin lines: results for the 64-atom ensemble.

ensemble is reflected only by the slight shift of the prepeak to lower wavenumbers and the existence of a small low-q shoulder.

Density is again shown to have only a modest influence on the structure factors, as can be seen from the comparison of the 64-atom results in figures 11 and 12. At the lower density we note a small ($\leqslant 0.1$ Å) shift in the position of the prepeak and a reduction of the height of the main peak in the number-density structure factor S_{NN}; otherwise the two results are completely identical.

3.2.4. Comparison with scattering experiments. X-ray or neutron scattering experiments measure an average of the partial structure factors, weighted with the corresponding scattering form factors. In the case of equiatomic K–Sn alloys, the difference in coherent neutron scattering lengths ($b_K = 0.36$, $b_{Sn} = 0.61$ [42]) leads to comparable weighting factors for all Bhatia–Thornton partials, so the prepeak in $S_{cc}(q)$ can be 'seen' in the neutron diffraction data. Figure 13 confronts theory and experiment [11] for the total neutron scattering structure factor and shows in addition the total x-ray scattering structure factor. Agreement is quite satisfactory, even excellent for larger momentum transfers ($q \geqslant 1.5$ Å^{-1}), for calculations based on the 64- and 96-atom ensembles at the experimental density. The prepeak reflecting the strong CSRO and strong Sn–Sn correlations is slightly affected by size effects: according to experiment, the prepeak is located at $q_p = 0.96$ Å^{-1}; in our simulations we find $q_p = 1.01$ Å^{-1} for the small and $q_p = 0.89$ Å^{-1} for the larger ensemble. Both simulations tend to underestimate the amplitude of the prepeak: according to experiment we have $S(q_p) = 1.11$ (at $T = 1185$ K);
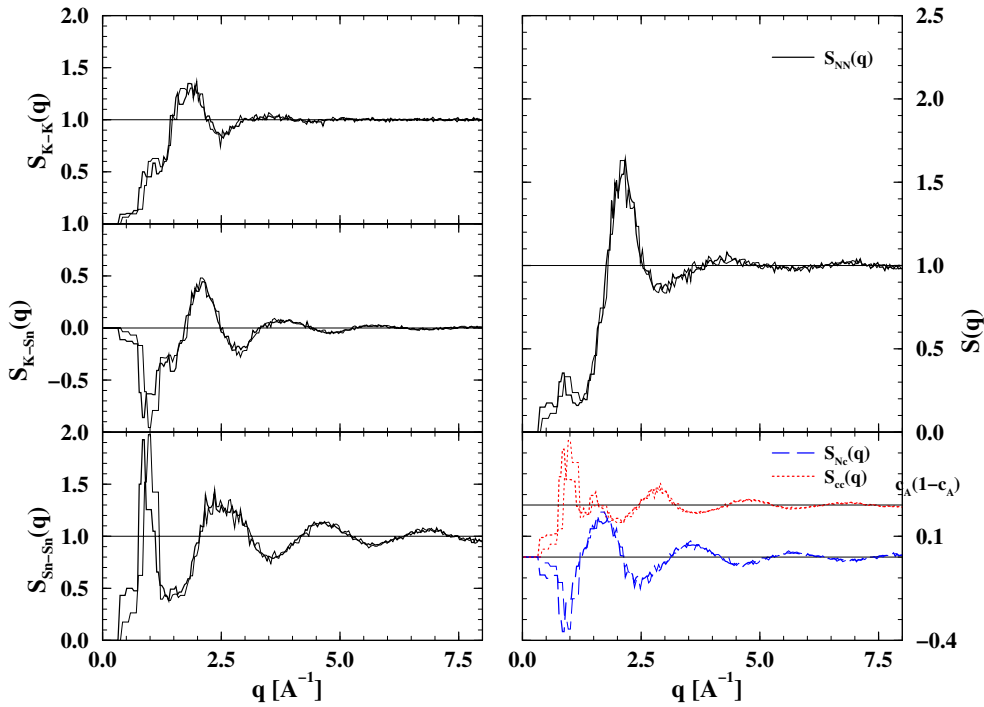
Figure 12. Partial static structure factors for molten K–Sn at $T = 1150$ K and $n = 0.023$ Å^3. Bold lines: results calculated for the 96-atom ensemble; thin lines: results for the 64-atom ensemble.

in both simulations we find $S(q_p) \sim 0.78$. For the more disordered state produced by the 124-atom ensemble, the amplitude of the prepeak is further reduced, without impairing the good agreement reached for higher wavenumbers. The main peak is situated at $q_1 = 2.26$ Å^{-1} for both theory and experiment. The amplitudes of the main peak and of the higher-order oscillations are in excellent agreement with experiment.

Simulations at the higher density for both the 64- and 124-atom ensembles do not lead to a very different picture. The only significant change is that the amplitude of the prepeak is reduced for the large ensemble to $S(q_p) \sim 0.5$, whereas that of the main peak is increased. Altogether it becomes evident that quite strong differences in the local order are reflected by only minor differences in the experimental neutron structure factors. Due to the large difference in the atomic numbers, the contribution of the S_{Sn-Sn} and S_{cc} structure factors is larger for x-ray scattering as demonstrated in figure 13. Hence an x-ray diffraction experiment could help to better characterize the local order in molten K–Sn alloys.

Our *ab initio* simulations lead to distinctly better agreement with the diffraction experiments than previous simulations based on the random packing of structural units (RPSU) and reference interaction site model (RISM) [11]. The RPSU model [43] assumes that the system consists of identical structural units or molecules (in our case these are the Sn$_4$ poly-anions), such that the total structure factor may be split into a molecular form factor for a single molecule and a second form factor expressing the correlations between molecular orientations, multiplied by the structure factor of the molecular centres. An interaction site is defined as a position within a molecule which locates the source of interactions with other centres. In the RISM, generalized Ornstein–Zernike equations are defined for the intermolecular site–site correlation functions and the intramolecular pair correlation functions [44, 45], these
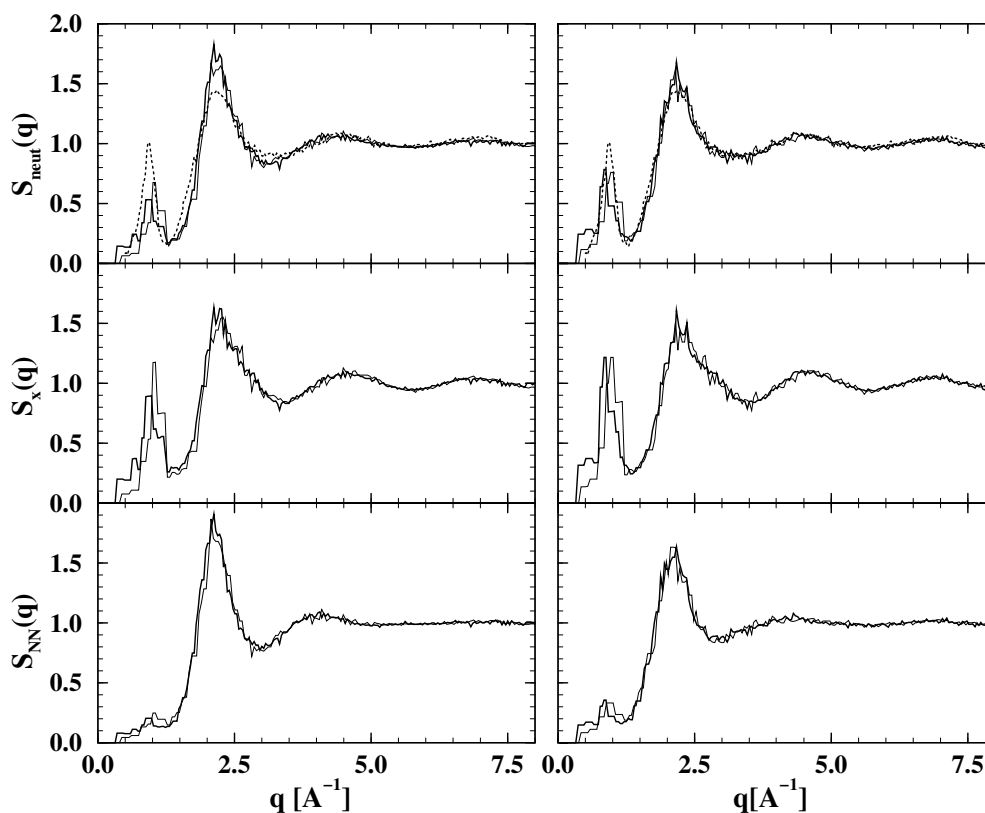
Figure 13. The total neutron-weighted static structure factor for liquid K–Sn at $T = 1150$ K. Dashed line: experimental result of Reijers *et al* [11]. In the left-hand panel, the bold solid line represents the results obtained with the 124-atom ensemble, the thin solid line those obtained with the 64-atom ensemble; $n = 0.026$ Å^{-3}. The right-hand panel shows the results obtained at $n = 0.023$ Å^{-3} for the 64-atom (thin lines) and 96-atom (bold lines) ensembles. For comparison the number-density structure factor $S_{NN}(q)$ and the total x-ray-weighted structure factor $S_X(q)$ are also shown (note that the contribution from concentration fluctuations to the total scattering is even larger for x-rays than for neutrons.

equations are then solved using a variational method. Although the fitting of the RPSU or RISM parameters allows reproduction of the shape of the prepeak and of the main peak, substantial deviations are found at small wavenumbers, where both models lead to density and concentration fluctuations that are too strong, and at larger wavenumbers, where the calculated structure factor is definitely out of phase with the experimental data. This indicates that the dynamical equilibrium between polyanions (which are continuously broken and reformed) and more disordered parts of the ensemble is essential for achieving good agreement with experiment.

It has been pointed out that the ratio q_p/q_1 may be used to characterize the variation in the liquid structure of alloys where in the crystalline state a transition from ionic to polyanionic bonding is observed. In typically saltlike systems such as Li–Pb, $q_p/q_1 \simeq 0.64$ (see, e.g., Ruppersberg and Egger [46]) has been found, whereas in K–Pb with a polyanionic structure at least in the crystalline state, a significantly smaller value of $q_p/q_1 \simeq 0.46$ has been reported [9, 10]. For liquid K–Sn, the neutron diffraction experiment yields an even smaller value of $q_p/q_1 \simeq 0.44$, whereas the LDA calculations yield $q_p/q_1 \simeq 0.40$ to 0.45 depending

on the choice of the ensemble and, to a lesser degree, on density. The significance of this correlation becomes clear if one remembers that $\lambda_p = 2\pi/q_p$ reflects the correlation length of the ordering effects giving rise to the prepeak; hence q_p/q_1 expresses this correlation length on the scale of the average interatomic distances. This correlation length is of course larger for ordering effects involving polyanion formation than for single-ion charge ordering.

The neutron diffraction data have also been used to characterize the short-range correlations in real space. The reduced total radial distribution function

$$G(R) = 4\pi R n(g(R) - 1)$$

obtained by Fourier transforming the measured total structure factor is compared in figure 14 with the corresponding theoretical result for the 96-atom ensemble calculated in terms of a weighted average over the partial pair correlation functions. The position of the first two peaks at $R = 2.97$ Å and $R = 3.69$ Å compares very well with the peak in the Sn–Sn and K–Sn correlation functions ($R = 2.93$ Å and $R = 3.63$ Å, respectively). A weak maximum (or rather plateau) around $R \sim 4.5$ Å does not correspond to the peak in the K–K correlation function (which overlaps with the more pronounced maximum in g_{K-Sn}), but results from the almost linear increase in g_{Sn-Sn} between 4.5 Å and 6 Å, which also leads to the weak second maximum in $g_{cc}(R)$ (cf. figure 7). The peaks in $G(R)$ have been fitted by a set of three Gaussians, the area under each Gaussian determining the corresponding partial coordination number. The values determined in that way agree rather well with our theoretical results (cf. table 2): $N_{Sn-Sn} = 1.8$ (experiment), $N_{Sn-Sn} = 1.9$ to 2.4 (theoretical, calculated for the small and large ensembles by integrating over the symmetric part of the first peak in the partial correlation function, respectively) and $N_{K-Sn} = 7.2$ (experiment), $N_{K-Sn} = 5.3$ to 7.0 (theory). The fact that both theory and experiment predict Sn–Sn coordination numbers smaller than 3 suggests that not all Sn atoms are part of complete Sn_4 tetrahedra, confirming our previous analysis.
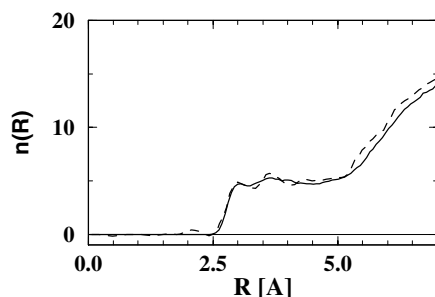

Figure 14. The total neutron-weighted reduced radial distribution function $G(R)$ for liquid K–Sn: solid line: theory (results calculated for the 96-atom ensemble); broken line: experiment.

3.3. Atomic dynamics

The single-particle dynamics in liquid K–Sn has been studied by calculating the velocity autocorrelation functions $VACF(t) = \langle\langle \vec{v}_l(t) \cdot \vec{v}_m(0) \rangle\rangle$ (the double brackets indicating averaging over the atoms l, m in the ensemble and over different starting points of the simulation) and their Fourier transforms, the frequency distribution functions $\Psi(\omega)$. If only atoms of one species are considered, the partial VACFs and frequency distributions $\Psi_i(\omega)$, $i = K$, Sn, are obtained. Because of the still limited time span of the MD runs and the statistical fluctuations arising from the small size of the ensembles, a filter-function approach has to be used in performing the Fourier transform in order to achieve a reasonably smooth spectrum.

The results compiled in figures 15 and 16 illustrate the very different character of the motions of K and Sn atoms in the molten alloy: the K–K velocity autocorrelation function shows a deep minimum following a steep initial decay and strongly damped long-time behaviour. This behaviour is indicative of a strong 'cage effect'—collisions with nearest-neighbour atoms leading to a reversal of the direction of motion after a short interval of time. In the partial frequency distribution (see figure 16) this is reflected by a strong vibrational component centred around $\sim$16 ps^{-1}, corresponding to a characteristic period of about 0.4 ps of the K vibrations. The Sn–Sn velocity autocorrelation function shows a much weaker cage effect and a pronounced long-time tail. In the frequency distribution we identify a dominant low-frequency peak at $\sim$5 ps^{-1}, a second broad peak near 20 ps^{-1} and a high-frequency shoulder at $\sim$35 ps^{-1}. We tentatively assign the low-frequency modes to translational or librational movements of Sn$_4$ polyanions or fragments thereof, the high-frequency mode to internal vibrations of Sn atoms within the Sn$_4$ tetrahedra and the medium-frequency modes to oscillatory movements of Sn atoms unbound to polyanions and linked only to fragments of tetrahedral anions. We note that the value of the high-frequency mode agrees reasonably well with that of optical phonons in α-tin, whereas the broad medium-frequency peak spans the range covered by transverse and longitudinal zone-boundary modes. Experimental investigations of the collective dynamics of molten alloys using inelastic neutron scattering are very scarce. For molten K–Pb, Price [47] measured a generalized vibrational density of states and identified two distinct inelastic peaks. The lower one was associated with librational motions of Pb$_4$ tetrahedra, that at higher frequency with internal vibration in the tetrahedra. This interpretation agrees with our present results.
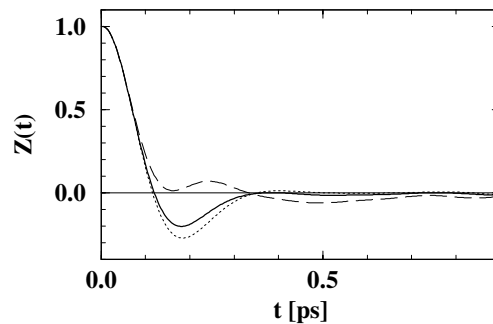

Figure 15. Velocity autocorrelation functions $Z(t)$ for liquid K–Sn at $T = 1150$ K, calculated for the 96-atom ensemble at $n = 0.023$ Å^{-3}. Solid line: total; broken line: Sn–Sn; dotted line: K–K correlation functions.

The frequency distributions do not show any dramatic size effect or density dependence, except in the low-frequency limit characterizing the diffusional component of the atomic motions. In this range we note a rather pronounced difference between the high-density 64-atom ensemble representing the 'plastic' phase of KSn and the results obtained at lower density, quite independent of the number of particles in the ensemble. In the low-frequency limit, the partial frequency spectrum of the Sn atoms drops nearly to zero in the plastic phase, indicating that the diffusive motion of the nearly perfect Sn$_4$ polyanions has come to a nearly complete arrest.

Diffusion constants may be derived from the low-frequency limit of the frequency distributions
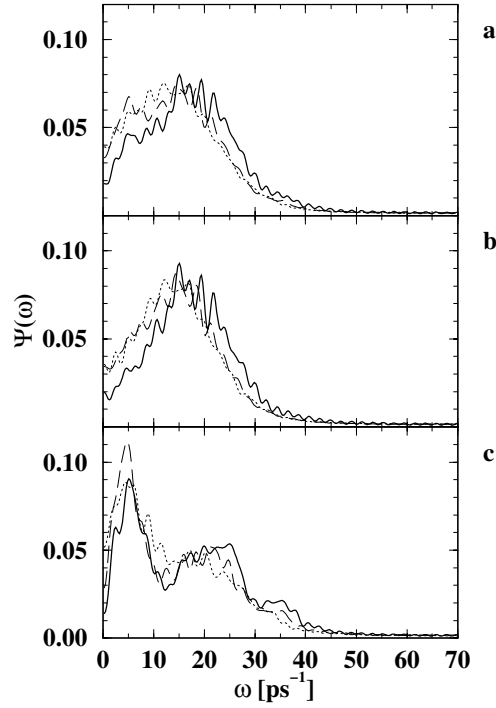
$$D_i = \frac{k_B T}{m_i} \Psi_i(0)$$

Figure 16. Frequency distribution functions $\Psi_i(\omega)$ for molten KSn at $T = 1150$ K: (a) total $\Psi(\omega)$; (b), (c): partial $\Psi_i(\omega)$, $i = $ K, Sn. Bold lines: $N_{at} = 64$, $n = 0.026$ Å^{-3}; thin lines: $N_{at} = 64$, $n = 0.026$ Å^{-3}; dotted lines: $N_{at} = 96$, $n = 0.023$ Å^{-3}.

or alternatively from the long-time behaviour of the mean square displacement functions $u^2(t) = \langle\langle(\vec{r}_l(t) - \vec{r}_l(0))^2\rangle\rangle$. The confrontation of the two sets of results represents a very critical test of the accuracy of the calculations. In making the comparison one has to keep in mind that in spite of the very long simulation times that we have used, the low-frequency limit of the vibrational spectrum is still quite sensitive to the technicalities of the Fourier transform of the VACFs. The mean square displacements on the other hand are really well converged, and the diffusion constants derived via this route should eventually be considered as slightly more reliable. Our results are compiled in table 3. For the small high-density ensemble representing the 'plastic' phase, we find a rather small total diffusion constant; the diffusion of the Sn atoms is slower than that of the K atoms by at least a factor of four. In this case the density has a substantial influence on the diffusive dynamics: in the low-density 64-atom ensemble, diffusion is nearly two times faster, the enhancement being more pronounced for Sn than for K. For the more disordered large 124-atom ensemble, the density dependence is less pronounced. In this case the presence of extra Sn atoms which cannot be accommodated in perfect Sn$_4$ tetrahedra prevents the formation of the plastic phase. At the experimental density of $n = 0.023$ Å^{-3} we note a quite good agreement between the simulations based on the 96- and 124-atom ensembles, except for the Sn diffusion constants where the higher degree of local order in the 96-atom ensemble is reflected by a lower value of the diffusion constant of Sn. The simulations based on the smaller 64-atom ensemble lead to a distinctly lower diffusivity; again that of the Sn atoms is most strongly affected. Our results show that a measurement of the interdiffusion constants could offer important complementary information on the existence of Zintl polyanions.

Table 3. Total and atom-specific diffusion constants for molten K–Sn alloys, calculated for ensembles with 64, 96 and 124 atoms and at two different densities. Results calculated from the time dependence of the mean square displacement (MSD) functions and from the low-frequency limit of the frequency distribution functions calculated in terms of the velocity autocorrelation functions (VACFs) are given. For comparison we note the diffusion constants of the pure metals at their respective melting points: $D_{Sn} = 0.18$ Å^2 ps^{-1} (ab initio MD), 0.20 Å^2 ps^{-1} (experiment, after reference [49]); $D_K = 0.42$ Å^2 ps^{-1} (ab initio MD), 0.36 Å^2 ps^{-1} (experiment, after reference [49]).

N_{at}	n (Å^{-3})	D_{tot} (Å^2 ps^{-1})		D_K (Å^2 ps^{-1})		D_{Sn} (Å^2 ps^{-1})	
		VACF	MSD	VACF	MSD	VACF	MSD
64	0.026	0.298	0.214	0.489	0.350	0.110	0.078
	0.023	0.527	0.415	0.834	0.631	0.225	0.198
96	0.023	0.638	0.623	0.884	0.860	0.399	0.387
124	0.026	0.443	0.456	0.591	0.542	0.297	0.370
	0.023	0.667	0.670	0.822	0.878	0.514	0.462

Compared to the diffusion constants of the pure liquid elements at their respective melting points (Sn: $T_m = 505$ K, $D_{Sn} = 0.20$ Å^2 ps^{-1} from experiment [49], $D_{Sn} = 0.18$ Å^2 ps^{-1} from ab initio simulations; K: $T_m = 337$ K, $D_K = 0.36$ Å^2 ps^{-1} from experiment [49], $D_K = 0.44$ Å^2 ps^{-1} from ab initio simulations [48]), the diffusion constants of both elements are strongly enhanced for the liquid alloy due to the much higher melting temperature. In the 'plastic' phase, the diffusivity of K remains comparable to that of the pure metal at its melting point, whereas the diffusion of Sn is slowed down by a factor of at least two, as diffusion is possible only through the exchange of Sn atoms among different polyanions (cf. also figure 2).

3.4. Electronic structure

3.4.1. Density of states. In I we have demonstrated that the polyanionic structure of the compound leads to a very peculiar character of the electronic band structure: the bands may be indexed according to the irreducible representation of the tetrahedral group (T$_d$, 432m). The Sn s states split into two bands corresponding to the molecular orbitals of the Sn^{4-} tetrahedra belonging to the irreducible $\Gamma_1(A_1)$ and $\Gamma_4(T_2)$ representations. The bonds derived from the Sn p states split into bonding linear combinations belonging to the $\Gamma_3(E)$, $\Gamma_4(T_2)$ and $\Gamma_1(A_1)$ irreducible representations and antibonding combinations with $\Gamma_5(T_1)$ and $\Gamma_4(T_2)$ symmetry. The Fermi level falls into the bonding/antibonding gap. If the polyanionic order is preserved in the liquid state, we expect the electronic density of states of the molten alloy to show a comparable structure.

The electronic density of states (DOS) of liquid K–Sn has been calculated for a series of selected instantaneous configurations and using a set of $\vec{k}$-points instead of the Γ point only (for the small ensemble we use a $4 \times 4 \times 4$ grid in the Brillouin zone of the computational supercell). Partial and angular-momentum-decomposed DOSs have been calculated by projecting each plane-wave component of an eigenstate on s, p, d spherical waves within atom-centred spheres (for technical details, see I).

Figure 17 shows the total, site-specific and angular-momentum-decomposed DOSs calculated for a series of seven well-ordered configurations of the 64-atom ensemble at a density $n = 0.026$ Å^{-3}. We find that in this case the electronic structure of the melt is very similar to that of the crystalline intermetallic compound, except for a modest disorder-induced broadening of all bands. The two lowest bands have a Sn s character; the occupation of these bands
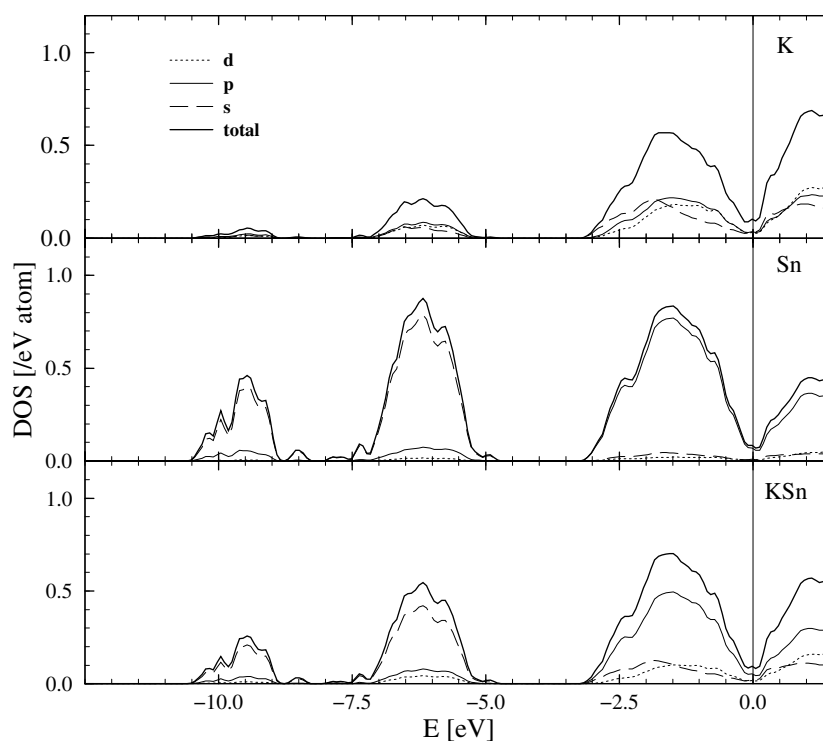
Figure 17. Total, partial and angular-momentum-decomposed electronic densities of states calculated for representative configurations of the 64-atom ensemble at $n = 0.026\,\text{Å}^{-3}$ representing the 'plastic' phase of KSn. Bold lines: total and partial (site-projected) DOSs; thin lines: s, p and d components (dashed, full and dotted respectively).

corresponds exactly to the 1:3 ratio expected on the basis of the dimensions of the irreducible representations of the tetrahedron group from which these bands are derived. The occupied band close to the Fermi level has pure p character in the Sn sites and strongly mixed s, p, d character on the K sites, suggesting that the DOS within the K spheres arises from extended Sn p states overlapping into neighbouring spheres rather than from the occupation of eigenstates derived from atomic K orbitals. Again this is very similar to the electronic structure of the crystalline compound. It is also remarkable that the narrow semiconducting gap ($E_g = 0.7\,\text{eV}$) of the crystalline phase survives as a very deep pseudogap at the Fermi level (the DOS at the Fermi level is only 0.08 states eV^{-1}/atom). Hence for the small high-density ensemble representing the 'plastic' phase of the alloy, the analysis of the electronic structure supports the existence of a high degree of polyanionic order in the 'rotor phase' of K–Sn.

   Figure 18 displays the total electronic DOS for a series of instantaneous configurations of the 96- and 124-atom ensembles at the experimental density, selected at equidistant time intervals. As expected from the analysis of the structural correlations, the weaker local ordering effects are reflected in a more pronounced smearing of all bands. The bimodal character of the Sn s band with the characteristic 1:3 weighting of the two subbands is well preserved, but due to the disorder-induced broadening of the bonding and antibonding p bands, the pseudogap at the Fermi level is filled even after a sufficiently long equilibration. In the more ordered 96-atom ensemble, the depth of the pseudogap is about 50% of the DOS maxima in the bonding and antibonding parts of the Sn p band; in the 124-atom ensemble it is somewhat shallower. A
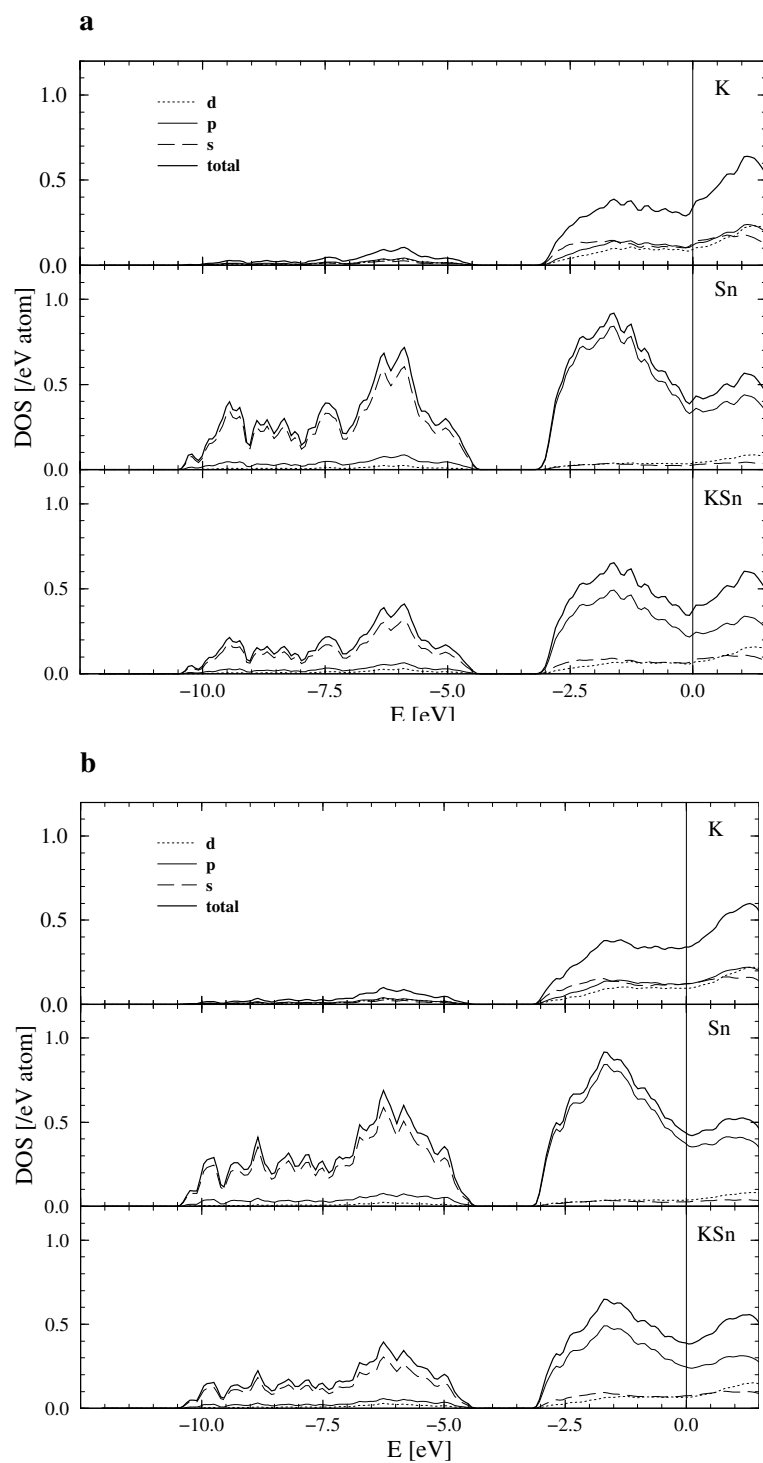
a

b

Figure 18. Total electronic densities of states for the 96- and 124-atom ensembles (parts (a) and (b), respectively) of K–Sn at $n = 0.023$ Å^{-3} representing the liquid phase; cf. figure 17.

detailed analysis of single configurations demonstrates that in well-ordered local configurations the splitting of the bands characteristic for a short-range tetrahedral polyanionic order is momentarily recovered, but the formation of intertetrahedral bands tends to produce states within the internal pseudogaps of both the Sn s and Sn p bands. Hence electron spectroscopy concentrating in particular on the electronic density of states at the Fermi level could in principle yield important additional information on the degree of local ordering present in the melt. However, it is clear that due to the reactivity of the alkali metals and the high vapour pressure of the alloy such an experiment will be very difficult.

3.4.2. Electron densities.   A very useful illustration of the polyanionic character of molten KSn comes from the analysis of the electron densities. Figure 19 shows equidensity contours of the electron densities corresponding to the upper part of the valence bands calculated for an instantaneous configuration of the small ensemble at high density. Part (a) of this picture confirms that in this 'plastic' state the electron-density distribution in the Zintl polyanions is very similar to that in the intermetallic compound: the valence electrons are concentrated around the Sn atoms; the surface of constant electron densities reflects the tetrahedral shape of the polyanions; K atoms are completely electron depleted. Compared to the crystalline intermetallic compound (cf. figure 7 in I) the electron-density contours are only slightly more diffuse, reflecting the more extended character of the electronic eigenstates and the influence of disorder. For the more disordered liquid-like configuration of the 96-atom ensemble (see part (b) of figure 19) the correctness of the Zintl picture is confirmed, although only a few nearly tetrahedral configurations are recognizable.

3.5. Summary for K–Sn

Our extended MD simulations shed new light on the controversial question of the existence of polyanions in liquid K–Sn alloys and—rather unexpectedly—also on the occurrence of a 'plastic' phase (often also referred to as a 'rotor' phase) with liquid-like behaviour of the alkali atoms only. This phase was formed in simulations at densities that are higher than that estimated from the diffraction data for the molten alloy. All Sn atoms form a regular array of Sn_4 tetrahedra which remain at fixed positions; the K atoms diffuse freely in the interstitial region. Only very occasional close contacts between neighbouring tetrahedra lead to a destruction of a tetrahedral cluster which is immediately recreated. In the electronic structure the high degree of polytetrahedral order is reflected in a very deep pseudogap at the Fermi level.

Simulations at the experimental density performed for three different ensembles produce a liquid-like phase with a degree of local order that depends to some degree on the ability of all Sn atoms to simultaneously arrange in electronically saturated polyanionic clusters. If the number of atoms is such that there are always excess Sn atoms, these behave as a very aggressive chemical species; their interaction with the polyanions leads to a reduction of the degree of local order. The results obtained with the more ordered 64- and 96-atom ensembles lead to excellent agreement with neutron diffraction data. However, it remains very difficult to quantify exactly the fraction of Sn atoms forming parts of long-lived Sn_4 polyanions.

4. Molten Na–Sn alloys

While in the K–Sn system the equiatomic compound KSn with the polyanionic structure is by far the most stable one, in the Na–Sn system an isostructural (NaPb-type) poly-anionic compound NaSn coexists with several compounds with a near-octet stoichiometry (e.g. $Na_{15}Sn_4$). The electronic structure of the isostructural and isoelectronic near-octet
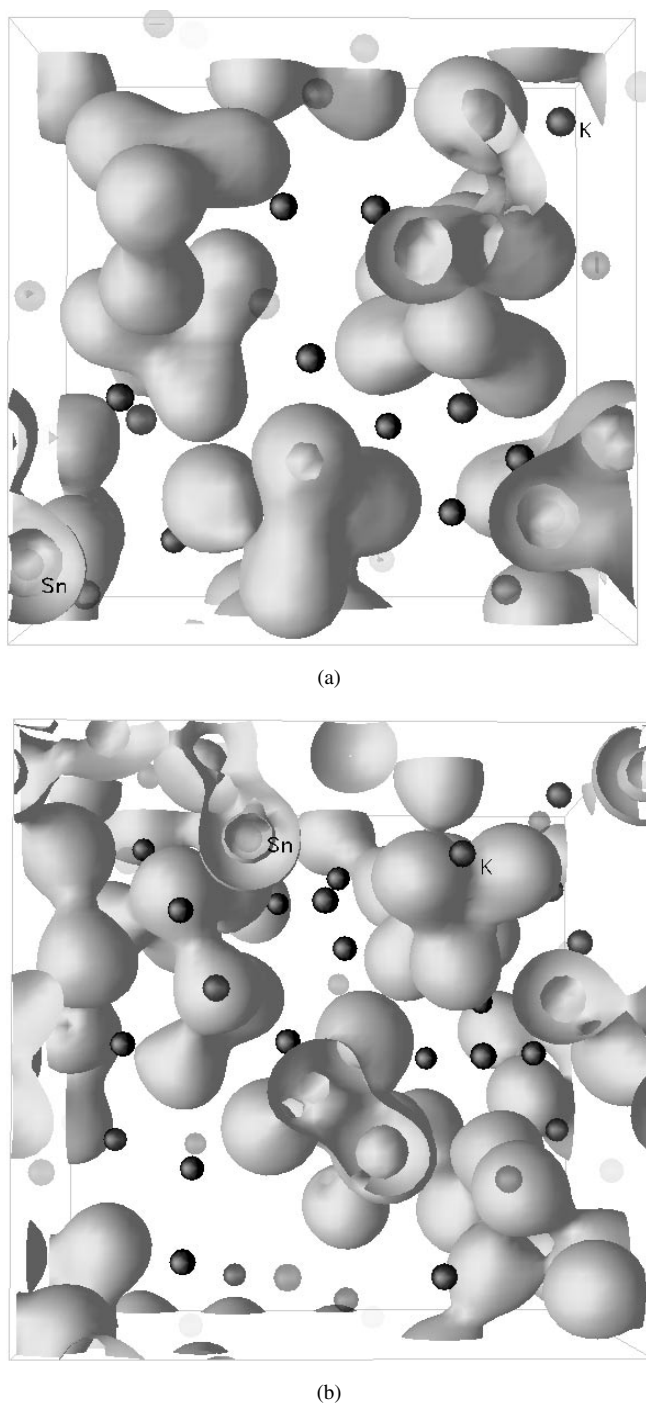
(a)

(b)

Figure 19. Constant-electron-density contours calculated by integrating over the upper part of the valence band ($\sim$−3.5 eV to E_F) of molten K–Sn. Small dark balls represent K atoms. At the boundaries of the simulation box, the constant-density surfaces are cut open. Part (a) shows an instantaneous configuration of the 64-atom ensemble at high density, part (b) a configuration of the 96-atom ensemble at the experimental density.

compound $Na_{15}Pb_4$ has been discussed by Tegze and Hafner [50] and the essentially ionic character of the chemical bond has been confirmed. For the equiatomic NaPb and NaSn compounds, semiconducting gaps of 0.3 eV and 0.4 eV have been reported (see I and reference [50]). For molten Na–Sn alloys, anomalies in the electronic transport properties and in the thermodynamic excess functions have been reported at the equiatomic and the octet compositions, suggesting that a similar competition between polyanionic and ionic ordering exists also in the molten phase. The broad plateau in the electrical resistivity extending between the equiatomic and the octet compositions suggests a gradual transition from charge ordering in the Na-rich limit to eventually some degree of polyanionic ordering in the 50/50 composition range.

Simulations for liquid NaSn have been performed for a 124-atom cell and extended over about 20 ps. The equilibrium atomic volume calculated at $T = 850$ K is $\Omega = 28.60$ Å^3, corresponding to an excess volume of $\Delta\Omega = -14.7\%$ compared to a volume contraction of $\Delta\Omega = -18.4\%$ calculated for the crystalline intermetallic compound. We note that the difference in excess volume of the liquid and solid phases is considerably smaller than in the case of KSn. The estimated liquid density and the expansion relative to the crystal ($\Delta\Omega = +4.5\%$) are in reasonable agreement with the density estimated from the diffraction data of Alblas *et al* [5]. Note that the LDA error is smaller than for KSn, as already noted for the crystalline intermetallic compounds. In contrast to the K–Sn system where the approach to equilibrium was found to be very slow, the Na–Sn system approached a steady state rather quickly. The MD simulation was stopped after about 20 ps, as no further evolution in the structural and electronic properties and in the atomic dynamics could be detected.

4.1. Atomic structure

4.1.1. Pair correlations and angular correlations. The partial pair correlation functions for liquid NaSn are plotted in figure 20. Although at first glance the component-related pair correlations resemble those calculated for l-KSn, some characteristic differences are evident:

  (i) The ratio of first and second peak positions is now much more hard-sphere-like (we calculate $R_2/R_1 \sim 1.77$ for the Na–Na correlation, and $R_2/R_1 \sim 1.91$ for both Na–Sn and Sn–Sn correlations).
 (ii) The peak heights of the Na–Sn and Sn–Sn pair correlations are now nearly equal.
(iii) Partial coordination numbers calculated by integrating over the symmetric part of the first peak (see table 4) show a reduced number of neighbours around Na—evidently as a consequence of the smaller atomic size. The Sn–Sn coordination number is slightly higher than in l-KSn.
(iv) The reduced size ratio is also reflected in the Bhatia–Thornton pair correlation functions: $g_{cc}(R)$ reflects the dominance of heterocoordinations in the nearest-neighbour shell, the hard-sphere-like form of $g_{NN}(R)$ the absence of significant topological short-range ordering effects and the smaller amplitude of $g_{Nc}(R)$ a weaker coupling of density and concentration fluctuations.

The ordering effects being weaker in l-NaSn than in l-KSn is confirmed by the analysis of the angular correlations. We proceed in the same way as for KSn, searching for each Sn atom for the three shortest Sn–Sn distances which potentially belong to Sn_4 tetrahedra and determining the angles formed between these three bonds. The result given in figure 21 for a characteristic configuration shows a spread of the Sn–Sn distances comparable to that in K–Sn (as expected from the width of the first peak in the correlation function), but only a few Sn–Sn–Sn angles close to 60°. The frequent occurrence of angles scattered around 120°
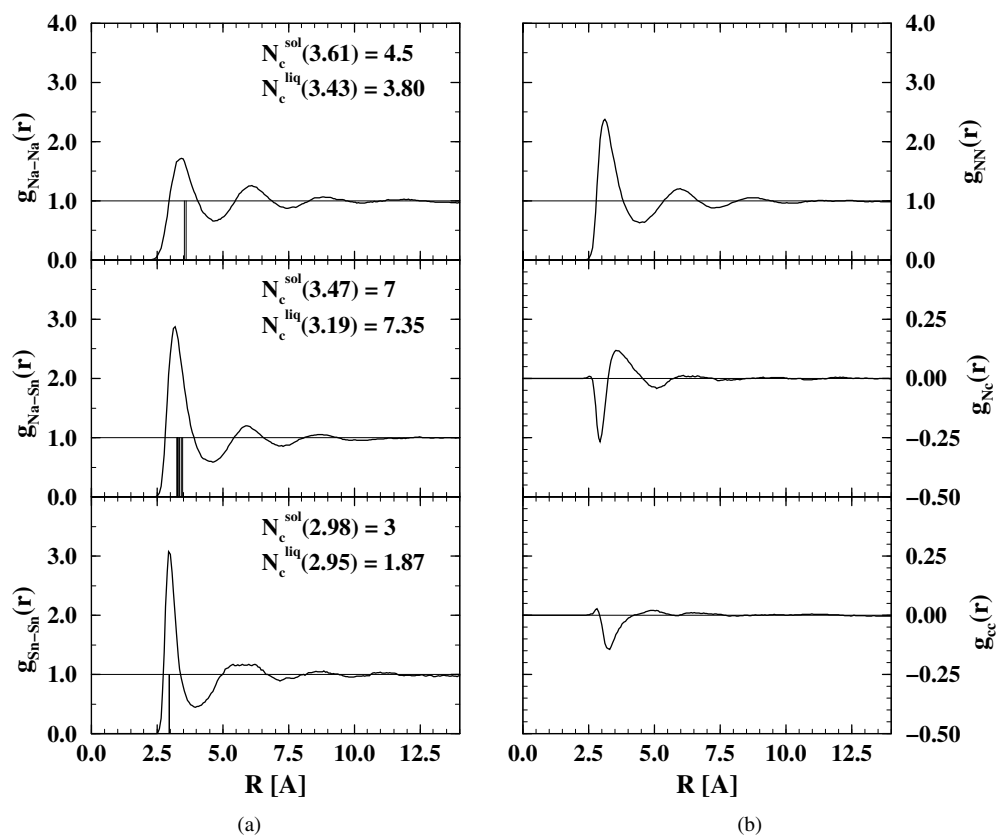
Figure 20. Pair correlation functions $g_{\text{Na}-\text{Na}}(R)$, $g_{\text{Na}-\text{Sn}}(R)$, $g_{\text{Sn}-\text{Sn}}(R)$ (a) and $g_{NN}(R)$, $g_{Nc}(R)$ and $g_{cc}(R)$ (b) for liquid NaSn at $T = 850$ K.

Table 4. Partial coordination numbers for liquid and crystalline Na–Sn alloys.

	Crystal		Liquid alloy	
	N_{ij}	R_{max}[a] (Å)	N_{ij}	R_{max}[a] (Å)
Na–Na	4.5	3.61	3.80	3.43
Na–Sn	7.0	3.47	7.35	3.19
Sn–Sn	3.0	2.98	1.87	2.95

[a] R_{max} stands for the largest nearest-neighbour distance in the crystalline structure and for the position of the first peak in the pair correlation function, respectively.

suggests that the distribution of the Sn atoms is dominated by close-packing requirements, modified by chemical ordering.

A projection of an instantaneous configuration is shown in figure 22. No Sn tetrahedra can be found; the Sn atoms instead form a dense three-dimensional network (but remember that the K–Sn bonds are only marginally longer than the Sn–Sn bonds). In this respect our result for NaSn is similar to the *ab initio* MD results of de Wijs *et al* [22] for Cs–Pb and of Seifert *et al* [20, 23–25] for l-NaSn (but see below for a more detailed comparison); they also concluded that the anions form an entangled, rather irregular network rather than regular, isolated polyanions.
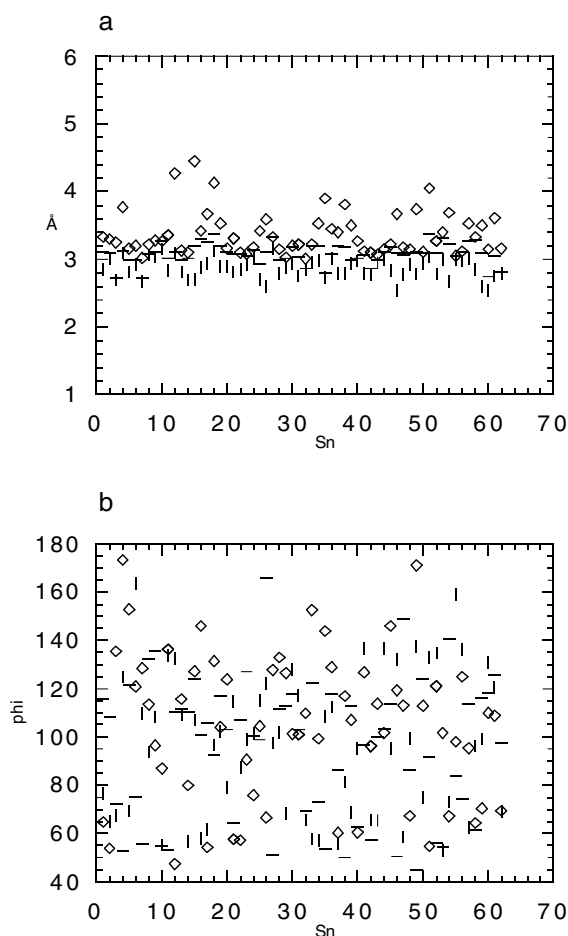
a

b

Figure 21. (a) The distribution of the three shortest Sn–Sn bonds around each Sn atom and (b) the distribution of the Sn–Sn–Sn bond angles calculated for a characteristic configuration of the 124-atom ensemble representing l-NaSn.

4.1.2. Partial structure factors and diffraction data.   Figure 23 represents the partial structure factors for l-NaSn. Compared to the case for l-KSn we find:

(i) There are larger amplitudes of the main peaks of all three structure factors.
(ii) There is a less pronounced 'prepeak' in $S_{Sn-Sn}(q)$, although the minimum in $S_{Na-Sn}(q)$ at the same wavenumbers is as deep as for K–Sn.
(iii) There is a prepeak instead of a shoulder in $S_{Na-Na}(q)$.
(iv) In the Bhatia–Thornton partial structure factors we notice the complete absence of a prepeak in $S_{NN}(q)$. Combined with stronger higher-order oscillations this confirms the hard-sphere-like character of the density–density structure factor. S_{Nc} and S_{cc} show much weaker oscillations than in l-KSn, corroborating the reduction of local ordering noted above.

Figure 24 shows the neutron- and x-ray-weighted total structure factors, compared with the neutron diffraction data of Alblas *et al* [5]. Due to the similar coherent neutron diffraction lengths of Na and K ($b_{Na} = 0.36$, $b_{Sn} = 0.61$), the conditions for an experimental observation
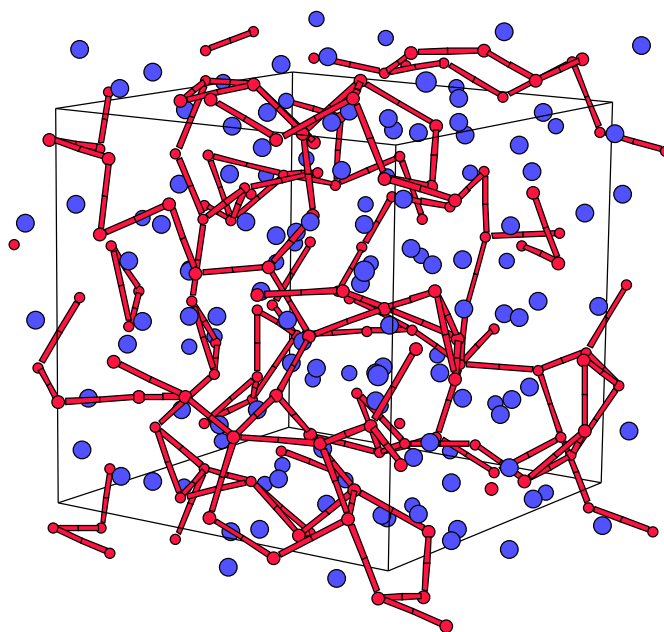
Figure 22. Projection of an instantaneous configuration of the 124-atom ensemble representing l-NaSn. Large spheres: Na atoms; small spheres: Sn atoms. Bars represent Sn–Sn nearest-neighbour bonds.
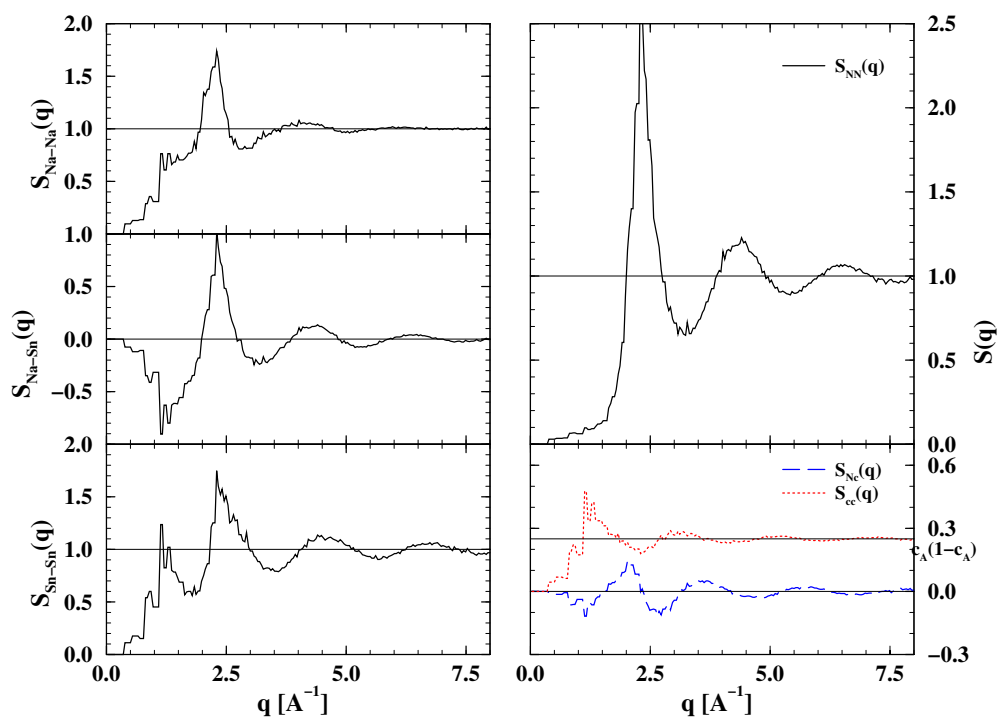

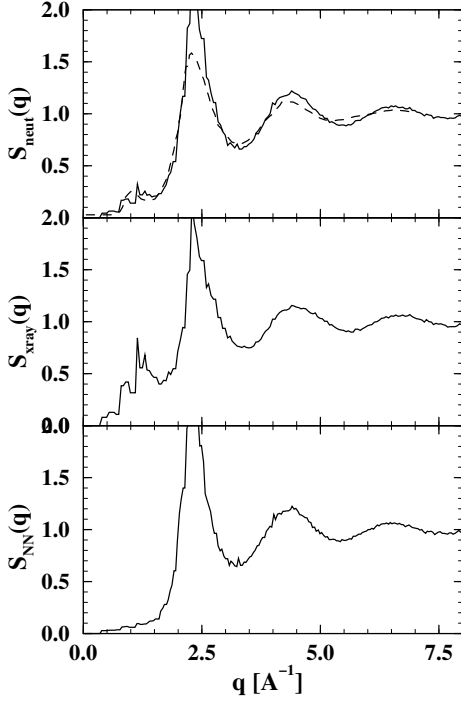**Figure 23.** Partial static structure factors for liquid NaSn at $T = 850$ K.

Figure 24. Total neutron- and x-ray-weighted static structure factors calculated for l-NaSn at $T = 850$ K. Solid line: theory; broken line: experiment.

of the short-range order are about the same as for K–Sn. However, we find that the less pronounced prepeak in $S_{\text{Sn}-\text{Sn}}$ largely cancels against the deep minimum in $S_{\text{Na}-\text{Sn}}$, so the neutron scattering structure factor is largely identical to $S_{NN}(q)$, except for the small hump near $q \simeq 1.1$ Å^{-1} originating from concentration fluctuations (preferred heterocoordination). The most pronounced discrepancy between theory and experiment is as regards the height of the main peak. This is possibly due to a slightly too high density resulting from the LDA. Otherwise, within the limits imposed by the smallness of the model, agreement between theory and experiment can be considered as satisfactory. A better 'visibility' of the short-range-order effects would be offered by x-ray diffraction, because in this case the diffraction intensity would be dominated by the contraction from the heavier Sn atoms. From the positions of the prepeak and of the main peak in the neutron structure factor, we calculate a ratio of $q_p/q_1 = 0.48$ (theory) and $q_p/q_1 = 0.45$ (experiment) which, according to the arguments given above, has been interpreted as evidence for a similar local order in l-NaSn and l-KSn. However, such a conclusion is in evident contrast with the different amplitudes of the partial structure factors and with our analysis of the angular correlations.

4.2. Atomic dynamics

Total and partial velocity autocorrelation functions and frequency distribution functions for l-NaSn are plotted in figure 25. For the Na atoms, the single-particle dynamics is again dominated by a strong cage effect, leading to a rather narrow band of vibrational modes centred at about 4 THz and a relatively weak diffusional component. The spectrum of the Na vibrations in NaSn is similar to that of K atoms in l-KSn, scaled by the square root of the mass ratio $\sqrt{M_K/M_{\text{Na}}}$. The dynamics of the Sn atoms, however, reflects the different local order in the two molten alloys: for Sn atoms in l-NaSn the velocity autocorrelation function of the
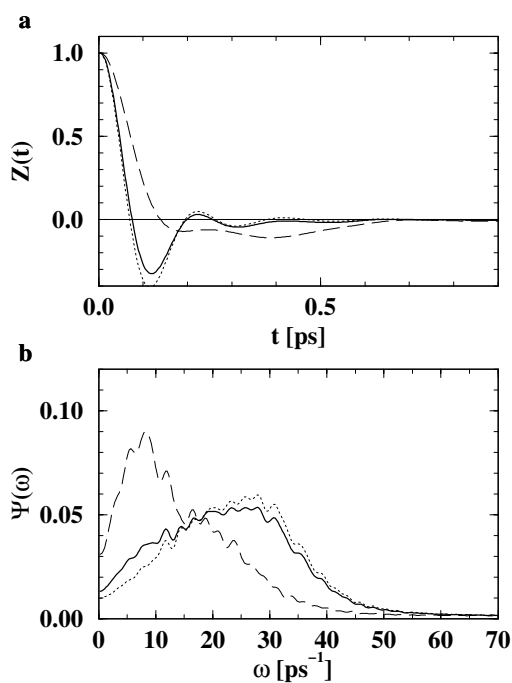
a

b

Figure 25. Velocity autocorrelation functions $Z(t)$ (a) and the frequency distribution function $\Psi(\omega)$ (b) for liquid Na–Sn at $T = 850$ K. Solid lines: total; broken lines: Sn–Sn; dotted lines: Na–Na correlation functions and frequency distributions.

tin atoms shows only weak long-time oscillations following the initial decay; $Z_{Sn}(t)$ remains negative for a long time following the reversal of the direction of motion. This indicates that although there are strong restoring forces driving the Sn atoms back to their initial positions, this does not lead to the excitation of rather well-defined vibrational states such as in l-KSn, but only to strongly overdamped Sn motions. This is also confirmed by the frequency distributions: in l-NaSn the single-particle dynamics of the Sn atoms is dominated by a single low-frequency peak at $\sim$1.2 THz with a shoulder close to $\sim$3.3 THz, in contrast to the strongly structured Sn frequency distribution in l-KSn. Thus the analysis of the single-particle dynamics supports the existence of a higher degree of topological Sn–Sn short-range order in l-KSn, but not in l-NaSn.

The diffusion constant calculated from the velocity autocorrelations (D(VACF) $=$ 0.25 $\text{Å}^2\,\text{ps}^{-1}$) compares well with the value derived from the mean square displacement functions (D(MSD) $= 0.22\ \text{Å}^2\,\text{ps}^{-1}$). Comparing with the results obtained for l-KSn using the same large ensemble, diffusion is slower in l-NaSn, clearly as a consequence of the increased density resulting from the smaller size of the alkali atom. From the time-dependent mean square displacements, we find $D_{Na} = 0.26\ \text{Å}^2\,\text{ps}^{-1}$ and $D_{Sn} = 0.19\ \text{Å}^2\,\text{ps}^{-1}$. This means that the ratio of the diffusion constants of the alkali and the Sn atoms is reduced in comparison to that for l-KSn. The explanation is that Sn–Sn bonding is weaker in l-NaSn and hence the Sn atoms can diffuse faster. Hence the investigation of the single-particle dynamics confirms the conclusions drawn from the structural analysis: polyanionic ordering is considerably reduced in l-NaSn compared to l-KSn.

4.3. Electronic structure

A further confirmation of the breakdown of polyanionic ordering in molten NaSn comes from the analysis of the electronic structure and charge densities. Figure 26 shows the total, partial and angular-momentum-decomposed electronic DOS calculated for a series of instantaneous
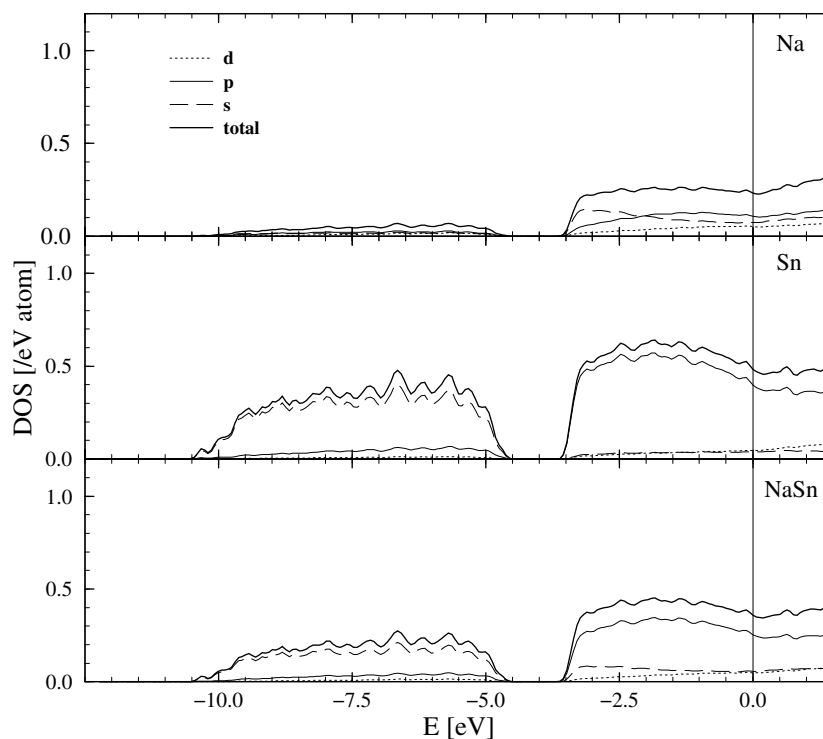
Figure 26. Total, partial and angular-momentum-decomposed electronic densities of states in liquid NaSn at $T = 850$ K. For the explanation of the notation, see figure 18.

configurations of l-NaSn. The characteristic result is the absence of a pseudogap at the Fermi level and of any splitting of the low-lying valence band of predominant Sn s character. For NaSn there is definitely more similarity of the electronic DOS of the molten alloy with that of crystalline phases in a hypothetical LiSn or CsCl structure than with the DOS of the stable polyanionic compound (cf. figures 3 and 8 in I). We emphasize that for l-NaSn we do not observe the fluctuations in the electronic spectrum associated with the dynamical formation and breaking up of well-ordered local configurations that is characteristic for l-KSn.

Finally we examined again the electron-density distributions. Figure 27 presents equidensity contours calculated for an instantaneous configuration. There is clear evidence for the dominant role of Sn–Sn bonding, but the Sn atoms form an entangled network rather than regular polyanions. We also note that in many Sn–Sn pairs, the overlap of the electron densities is much weaker, reflecting the reduced covalent character of the Sn–Sn bands.

4.4. Comparison with previous ab initio simulations

Liquid Na–Sn alloys of different compositions have been investigated by Seifert *et al* [20, 23–25] using Car–Parrinello MD simulations as well as tight-binding MD simulations. Our conclusion that in l-NaSn an entangled network of Sn is formed rather than well-defined isolated polyanions agrees with the conclusions of Seifert *et al*, but considerable differences exist in the calculated pair correlation functions, structure factors and in the electronic DOS. For the structure factor, Seifert *et al* find a strong and continuous increase of the prepeak with increasing Na concentration in the *ab initio* simulations, but not in the tight-binding
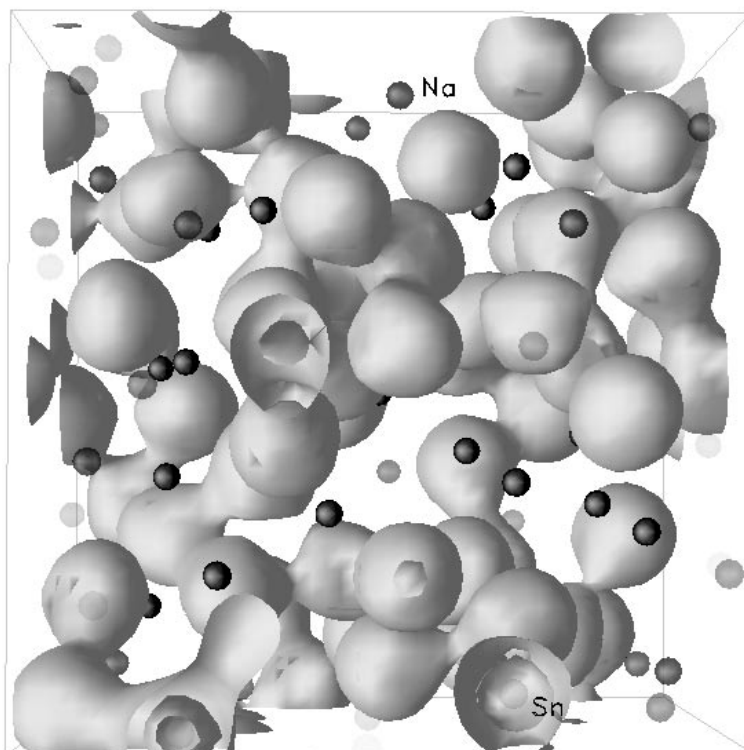
Figure 27. Constant-electron-density contours in an instantaneous configuration of molten NaSn, calculated by integrating over the upper half of the valence band ($E \leqslant -3.6$ eV). Small dark balls represent Na atoms.

simulations. This leads to a rather poor agreement with the experimental neutron diffraction data, also at equiatomic composition. This disagreement is probably to be attributed to a rather poor Na pseudopotential used in the calculations. In addition, Seifert *et al* find a very pronounced pseudogap in the electronic DOS of liquid NaSn at the Fermi level [25]—this is surprising in view of the absence of well-defined polyanions. This result is to be attributed to the use of a starting configuration in which all Sn atoms are part of ideal Sn_4 tetrahedra. The Car–Parrinello simulation also uses a much smaller time step of $\Delta t = 1.2$–2.4×10^{-16} s; the system was equilibrated over 5000 steps; production runs were extended over about 10 000 steps. This means that the total duration of a simulation was only about 2 ps. Our present experience excludes the possibility that equilibrium could possibly be reached in such short time intervals. The electronic structure reported in their paper essentially represents a smeared-out version of the electronic DOS of the initial configuration.

5. Molten Li–Sn alloys

Finally, to complete the series, we discuss very briefly the structural and electronic properties of liquid LiSn. In the crystalline state, LiSn forms a crystal structure intermediate between the polyanionic phases of the heavier alkali metals with the tetravalent elements and the saltlike (CsCl-type) structure of LiPb. The tendency to a simple ionic ordering is also reflected by the existence of several near-octet compounds (Li_7Sn_2, $Li_{22}Sn_5$, ...) of high stability. Both the

CsCl- and LiSn-type structures are considerably more compact than a hypothetical polyanionic (NaPb-type) LiSn compound, leading to a large volume contraction of $\Delta\Omega \simeq -27\%$ on alloying, compared to an excess volume of $\Delta\Omega \simeq -19.7\%$ in polyanionic LiSn (which is almost the same as that in NaSn). For the liquid alloy at 765 K we estimate an equilibrium volume of $\Omega = 22.13$ Å^3/atom and an alloying contraction of $\Delta\Omega = -15.8\%$. Hence we predict a considerable expansion on melting. Here we shall discuss only the main aspects of the atomic and electronic structures of l-LiSn that serve to illustrate the trends in the series KSn–NaSn–LiSn. A more detailed discussion of molten Li$_x$Sn$_{1-x}$ alloys with compositions ranging between the octet (Li$_4$Sn) and the equiatomic composition will be given elsewhere.

5.1. Atomic structure and dynamics

Figure 28 shows the partial pair correlation functions for liquid LiSn at $T = 765$ K. The trend observed on going from KSn to NaSn is continued: the height of the main Sn–Sn peak is further reduced while the main Li–Sn peak is higher than its counterpart in NaSn and KSn. While the position of the first peak in $g_{Sn-Sn}(R)$ remains almost unchanged ($R_1 = 2.98/2.95/2.93$ Å respectively in Li/Na/K–Sn), indicating a constant Sn–Sn bond length, the position of the second peak is shifted to smaller distances ($R_2 = 5.0/5.7/6.7$ Å in Li/Na/K–Sn), reflecting
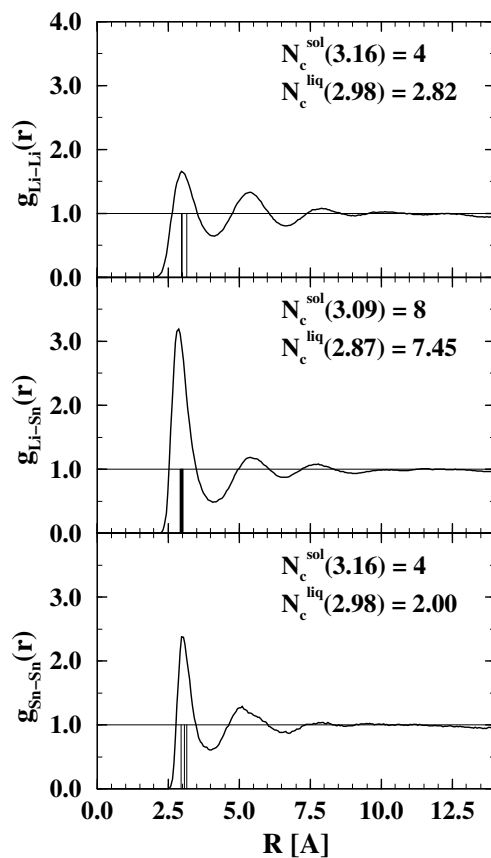

Figure 28. Partial pair correlation functions $g_{Li-Li}(R)$, $g_{Li-Sn}(R)$, $g_{Sn-Sn}(R)$ for liquid LiSn at $T = 756$ K.

the change from isolated polyanionic clusters to an entangled network of the polyvalent ions. In addition the Li–Sn distance as measured by the peak position in $g_{\text{Li–Sn}}(R)$ is shorter than both the Li–Li and Sn–Sn distances: $R_1^{\text{Li–Li}} = 2.98$ Å, $R_1^{\text{Sn–Sn}} = 2.98$ Å, $R_1^{\text{Li–Sn}} = 2.87$ Å— again a signature of saltlike bonding and short-range ordering. Table 5 summarizes the partial coordination numbers calculated either by integrating over the full peak up to the first minimum of the correlation function or by integrating over the symmetric part of the first peak, as well as the coordination numbers in the crystal. Either method of calculation yields a result similar to that found in the crystal: the Li–Li and Sn–Sn coordination numbers are about equal and smaller than half the Li–Sn coordination number. Angular correlations have been examined and found to be very similar to those in l-NaSn (see figure 21), showing a broad distribution over the range 60° to 180°.

Table 5. Partial coordination numbers of liquid and crystalline lithium–tin alloys. The coordination numbers for the liquid alloy have been calculated by integration the radial distribution function up to the first maximum and multiplying by two (corresponding to an integration over the symmetric part of the first peak, central column), and by integrating up to the first minimum (right-hand column).

	Crystal		Liquid alloy			
	N_{ij}	R_{max}[a] (Å)	N_{ij}	R_{max}[b] (Å)	N_{ij}	R_{max}[c] (Å)
Li–Li	4	3.16	2.82	2.98	5.55	4.13
Li–Sn	8	3.09	7.45	2.87	13.87	4.07
Sn–Sn	4	3.16	2.00	2.98	4.93	3.97

[a] Largest nearest-neighbour distance in the crystal.
[b] Position of first maximum in the partial pair correlation function.
[c] Position of first minimum in the partial pair correlation function.

The analysis of the partial structure factors (not shown here) confirms these trends: the prepeaks in the Sn–Sn and Li–Li structure factors are now of exactly the same height, the density-fluctuation structure factor $S_{NN}(q)$ is hard-sphere-like, $S_{cc}(q)$ has a prepeak at $q_p/q_1 \sim 0.55$, while $S_{Nc}(q)$ shows only very weak fluctuations demonstrating that concentration and density fluctuations are essentially decoupled.

Diffraction experiments using neutrons allow one to probe the chemical short-range order: due to the negative neutron scattering length of ^{7}Li, the weighting factors for the partial structure factors calculated using $b_{\text{Li}} = -0.233$ and $b_{\text{Sn}} = 0.61$ ($w_{NN} = 0.166$, $w_{NC} = 1.488$, $w_{cc} = 3.336$) favour the concentration fluctuations. Figure 29 shows the neutron- and x-ray-weighted total structure factors compared with $S_{NN}(q)$ and the experimental neutron diffraction data of Alblas *et al* [5]. This comparison confirms that our *ab initio* calculations lead to a correct description of the chemical short-range order in the melt. For the topological short-range order, x-ray diffraction data would represent a more serious test.

Figure 30 shows the projection of an instantaneous configuration of the 124-atom ensemble. Compared to l-NaSn, an even stronger entanglement of the Sn atoms, which show a tendency to form irregular clusters interconnected by chains of Sn–Sn bonds, is found. While in l-NaSn it was still possible to discern slightly distorted tetrahedra or fragments thereof embedded in the network of the Sn atoms, no such configurations are recognizable in l-LiSn. The tendencies of the Sn atoms to form a strong interconnected network in the liquid alloy is directly related to the formation of corrugated Sn layers in crystalline LiSn (cf. the discussion in I).

The single-particle dynamics in l-LiSn is similar to that observed in l-NaSn, but since the Li atoms are much lighter, the low-frequency Sn modes and the high-frequency Li modes are largely decoupled. Details will be given elsewhere [51].
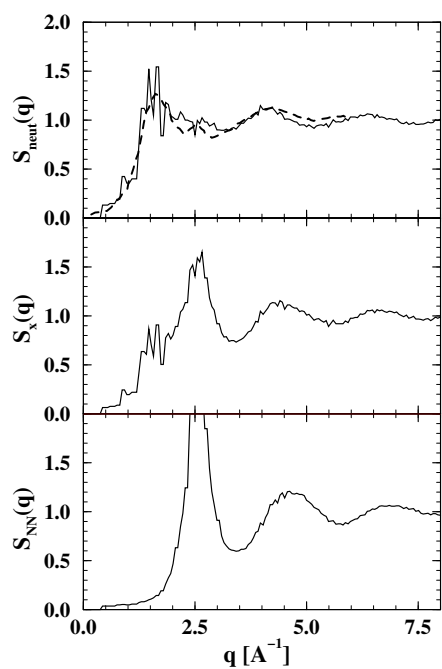
Figure 29. The total neutron- and x-ray-weighted total structure factor and number-density structure factor $S_{NN}(q)$ for liquid LiSn, compared with the neutron diffraction data of Alblas *et al* [5].
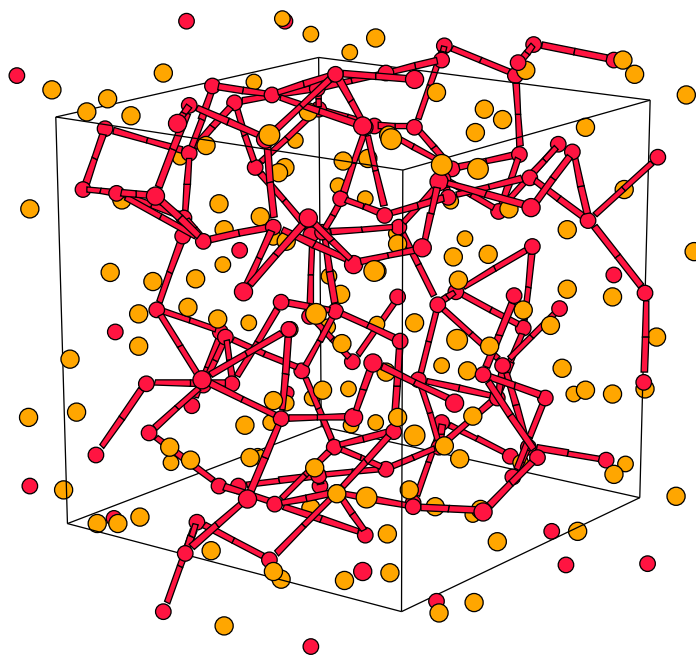

Figure 30. Projection of a characteristic instantaneous configuration of the 124-atom ensemble representing l-LiSn. Large light spheres: Li atoms; smaller dark spheres: Sn atoms. Bars mark Sn–Sn nearest-neighbour bonds.

5.2. Electronic structure

Figure 31 shows the electronic densities of states of l-LiSn. The electronic spectrum is very similar to that of crystalline LiSn and also resembles quite closely that of pure liquid Sn [51,52]. The essential difference is in both cases in the larger width of the internal gap separating the low-lying s band from the p band around the Fermi level. The reduction of both subband widths is due to the reduction of the effective Sn–Sn coordination number in the liquid alloy and due to the reduced s, p hybridization caused by disorder. We also note the close agreement—even in the details—with the electronic DOS of NaSn.
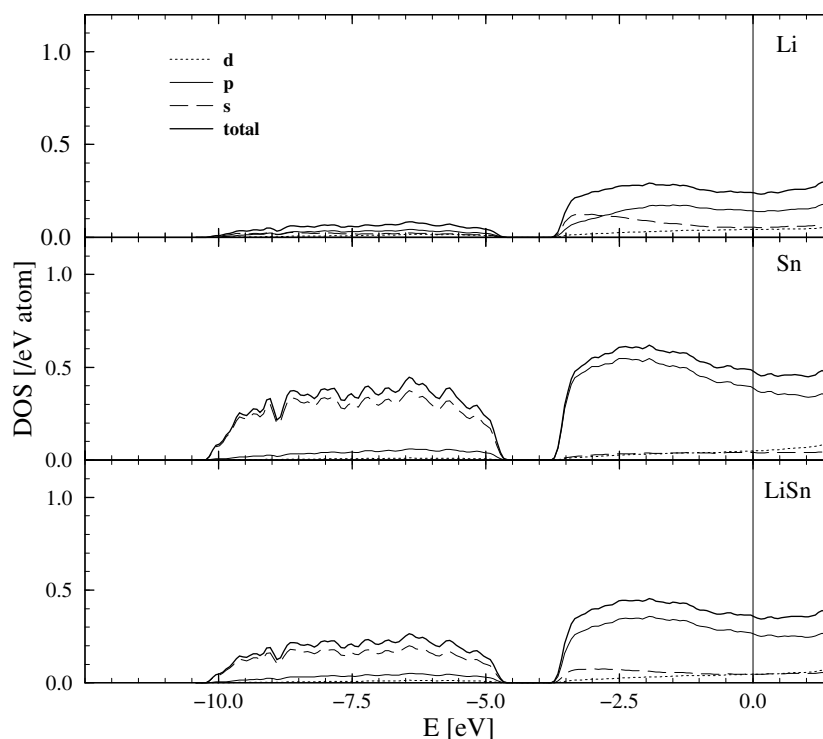

Figure 31. Total, partial and angular-momentum-decomposed electronic densities of states in l-LiSn at $T = 756$ K. See figure 18 for an explanation of the notation.

For l-Sn (where the calculated DOS is in very good agreement with photoelectron spectroscopy [53]) this peculiar form of the electronic DOS is remarkable because it signals the complete breakdown of sp hybridization characteristic for both crystalline (α and β) forms of Sn. The similarity of the DOS of l-Sn with that found for the molten alloys of Sn with Na and Li confirms that electronic properties and chemical binding are largely dominated by the more attractive Sn potential and that the alkali atoms play a rather minor role. However, in contrast to the case for l-KSn and the crystalline phases of KSn and NaSn, we also cannot identify any signature indicating the formation of polyanionic molecular orbitals.

6. Conclusions

Extended *ab initio* molecular dynamics simulations have been used to extend our studies of the stability of Zintl ions in crystalline alkali–tin compounds presented in I to the molten alloys.

We find that, in analogy to the crystalline phases, the tendency to form polyanionic clusters is stronger in alloys of the heavier alkalis than in those involving the lighter elements Na and Li. The reason is that only large alkali atoms surrounding the Sn clusters provide sufficiently large intercluster separations to inhibit the formation of intercluster bonds leading finally to an extended entangled network of Sn atoms instead of isolated Sn polyanions. Hence a certain fraction of Sn atoms form tetrahedral clusters in K–Sn, but not in Na–Sn and Li–Sn.

However, even for K–Sn, producing a clear picture on the basis of molecular dynamics simulations proved to be difficult. Our MD runs based on ensembles of different sizes, different densities and different starting configurations led to a consistent result only after being extended to timescales that are rather unusual even by the standards of the most advanced *ab initio* codes. At the experimental density, our simulations for ensembles with 64, 96 and 124 atoms demonstrated that at least a fraction of the Sn atoms arrange on electronically saturated Sn_4 polyanions if the system is allowed to equilibrate over sufficiently long times. Approach to equilibrium is particularly slow if the simulation is started from a configuration with strong heterocoordination. On the other hand, if a high degree of polyanionic order is present in the starting configuration, it decreases rather slowly on approaching equilibrium. The results are also sensitive to the exact number of Sn atoms: excess Sn atoms which cannot be accommodated on saturated Sn_4 tetrahedra act as a rather aggressive chemical species destabilizing already existing polyanions. In addition, the results show a certain dependency on the choice of the MD cell and on density.

At the estimated LDA equilibrium density, the simulations for a 64-atom ensemble of KSn at high density led to the formation of a 'plastic' or 'rotor' phase in which only the K atoms show liquid-like behaviour, whereas almost all Sn atoms form part of Sn_4 tetrahedra that perform only librational, but no diffusive motions. The arrangement of the Sn_4 tetrahedra in this 'plastic' phase is similar to that in the crystalline intermetallic compound. Simulations for a larger 124-atom ensemble at the same density did not produce this plastic phase, for two reasons: not all Sn atoms can simultaneously be part of polyanions; and the cubic shape of the MD cell does not allow for a favourable packing of the tetrahedral anions. Such a 'plastic' phase has been reported so far only for Cs–Pb and Na–Sn, but it would be surprising if it should not exist in K–Sn which definitely shows a higher degree of polytetrahedral order than Na–Sn. An experimental verification of the existence of the rotor phase would be very valuable.

At the density estimated from the experimental diffraction data, the simulations for all three ensembles converge to a liquid state and produce excellent agreement of the calculated neutron scattering structure factor and radial distribution function with experiment. Polyanionic order is considerably reduced compared to the 'plastic' phase, but still the existence of polyanions is essential for producing the correct position of the prepeak in the structure factor and is also reflected in the form of the electronic spectra. The presence of polyanions is also supported by the existence of inelastic peaks in the vibrational density of states. Experimental investigations of both the electronic and the vibrational spectrum would certainly be very valuable for a more precise assessment of the degree of polyanionic ordering in K–Sn and similar Zintl alloys.

Simulations for liquid Na–Sn and Li–Sn turned out to be a much simpler task. The MD runs converged much more quickly to a well-equilibrated liquid state with considerable chemical short-range order, the calculated static structure factors showing good agreement with experiment. No polyanions could be detected, but the strong binding between the Sn atoms led to the formation of a dense entangled network. The conclusion as to an absence of isolated polyanions is again supported by the analysis of the electronic and vibrational spectra. The low degree of polyanionic order suggests that the formation of a plastic phase during cooling will require very long equilibration times. We made several attempts to produce a plastic Na–Sn phase by high-temperature MD simulations of the crystalline phase. However,

for these still very small ensembles, even with the most favourable setting of the parameters of the Nosé thermostat, the temperature fluctuations are always at least of the same order as the temperature interval for which the existence of the rotor phase has been reported. Under these circumstances the chances of stabilizing the plastic phase are very poor.

The breakdown of polyanionic ordering in these alloys is clearly related to the small size of the alkali atoms: whereas in K–Sn the first peaks in the Sn–Sn and K–Sn pair correlation functions show only a very small overlap, with the result that the Sn–Sn clusters can be screened by a surrounding K shell, the overlap in the Sn–Sn and Na–Sn correlation functions is large in Na–Sn such that at the shortest distances hetero-atomic contacts already dominate. This tendency to a more saltlike charge ordering is even stronger in Li–Sn.

Altogether, however, the Zintl principle remains valid: bonding is dominated in all three alloys by the strong attractive Sn potential and the formation of at least partially covalent Sn–Sn bonds. The stability of a polyanion requires the covalent polyanionic bonds to be saturated, and this can only be achieved if intercluster contacts are suppressed by large alkali ions holding the clusters apart. Evidently this is difficult in the liquid phase, given the diffusive motions of the atoms. Therefore we find that in the liquid state the polyanions are rather short lived; they are continuously formed and rebroken after short time intervals.

Finally we would like to emphasize the technical aspects of our work demonstrating that *ab initio* simulations can now be performed at timescales sufficient for exploring complex chemical equilibria in molten alloys.

Acknowledgments

References

[1] Genser O and Hafner J 2001 *J. Phys.: Condens. Matter* **13**
[2] Zintl E and Bauer G 1933 *Z. Phys. Chem.* B **20** 245
[3] Price D L, Saboungi M L, Reijers H R J, Kearley G and White R 1991 *Phys. Rev. Lett.* **66** 1894
[4] Price D L, Saboungi M L and Howells W S 1995 *Phys. Rev.* B **51** 14 923
[5] Alblas B P, van der Lugt W, Dijkstra J, Geertsma W and van Dijk C 1983 *J. Phys. F: Met. Phys.* **13** 2465
[6] Reijers H R J, van der Lugt W and van Dijk C 1987 *Physica* B **144** 404
[7] Takeda S, Harada S, Tamaki S, Matsubara E and Waseda Y 1987 *J. Phys. Soc. Japan* **56** 3936
[8] Saboungi M L, Bromqvist R, Volin K J and Price D L 1987 *J. Chem. Phys.* **87** 2278
[9] Reijers H R J, van der Lugt W, van Dijk C and Saboungi M L 1989 *J. Phys.: Condens. Matter* **1** 5229
[10] Reijers H R J, Saboungi M L, Price D L, Richardson J W and Volin K J 1989 *Phys. Rev.* B **40** 6018
[11] Reijers H R J, Saboungi M L, Price D L and van der Lugt W 1990 *Phys. Rev.* B **41** 5661
[12] Stolz M, Leichtweiß O, Winter R, Saboungi M L, Fortner J and Howells W S 1994 *Europhys. Lett.* **27** 221
[13] Winter R 1997 *Thermodynamics of Alloy Formation* ed Y A Chang and F Sommer (London: The Minerals, Metals and Materials Society) p 143
[14] Avci R and Flynn C P 1979 *Phys. Rev.* B **19** 5967
[15] Madel O 1999 *Doctoral Thesis* TU Chemnitz
[16] Gremaud A *et al* 2001 *Helv. Phys. Acta* at press
[17] Howe M A and McGreevy R L 1991 *J. Phys.: Condens. Matter* **3** 577
[18] Stolz M, Winter R, Howells W S and McGreevy R L 1995 *J. Phys.: Condens. Matter* **7** 5733
[19] Galli G and Parrinello M 1991 *J. Chem. Phys.* **95** 7504
[20] Seifert G, Pastore G and Car R 1992 *J. Phys.: Condens. Matter* **4** L179
[21] de Wijs G A, Pastore G, Selloni A and van der Lugt W 1993 *Phys. Rev.* B **48** 13 459

[22] de Wijs G A, Pastore G, Selloni A and van der Lugt W 1994 *Europhys. Lett.* **27** 667
     de Wijs G A, Pastore G, Selloni A and van der Lugt W 1995 *J. Chem. Phys.* **103** 5031
[23] Schöne M, Kaschner R and Seifert G 1995 *J. Phys.: Condens. Matter* **7** L19
[24] Kaschner R, Schöne M, Seifert G and Pastore G 1996 *J. Phys.: Condens. Matter* **8** L653
[25] Seifert G, Kaschner R, Schöne M and Pastore G 1998 *J. Phys.: Condens. Matter* **10** 1175
[26] Villars P and Calvert N D 1985 *Pearson's Handbook of Crystallographic Data for Intermetallic Phases* vols
     1–3 (Metals Park, OH: American Society for Metals)
[27] Kresse G and Hafner J 1993 *Phys. Rev.* B **48** 13 115
     Kresse G and Hafner J 1994 *Phys. Rev.* B **49** 14 251
[28] Kresse G and Furthmüller J 1996 *Comput. Mater. Sci.* **6** 15
     Kresse G and Furthmüller J 1996 *Phys. Rev.* B **54** 11 196
[29] Nosé S 1984 *J. Chem. Phys.* **81** 511
[30] Allen M P and Tildesley D J 1990 *Computer Simulation of Liquids* (Oxford: Oxford University Press)
[31] Andersen H C 1980 *J. Chem. Phys.* **72** 2884
[32] Parrinello M and Rahman A 1980 *Phys. Rev. Lett.* **45** 1196
     Parrinello M and Rahman A 1981 *J. Chem. Phys.* **52** 7182
[33] Ray J R and Rahman A 1984 *J. Chem. Phys.* **80** 4423
[34] Teçza G W and Hafner J 1996 *J. Non-Cryst. Solids* **202** 1
[35] Price D L, Saboungi M L, Reijers H T J, Kearley G and White R 1991 *Phys. Rev. Lett.* **66** 1894
[36] Price D L and Saboungi M L 1991 *Phys. Rev.* B **44** 7289
[37] Saboungi M L, Fortner J, Howells W S and Price D L 1993 *Nature* **365** 237
[38] Reijers H T J, Saboungi M L, Price D L and van der Lugt W 1990 *Phys. Rev.* B **41** 5661
[39] Müller W and Stöhr J 1977 *Z. Naturf.* b **32** 631
[40] Bhatia A B and Thornton D E 1975 *Phys. Rev.* B **2** 3004
[41] Pearson W B 1972 *The Crystal Physics and Chemistry of Metals and Alloys* (New York: Wiley)
[42] Bacon G E 1972 *Acta Crystallogr.* A **28** 357
[43] Moss S C and Price D L 1985 *Physics of Disordered Materials* ed D Adler, H Fritzsche and S R Ovshinsky
     (New York: Plenum) p 77
[44] Chandler D and Andersen H C 1972 *J. Chem. Phys.* **57** 1930
[45] Hansen J-P and McDonald I R 1986 *Theory of Simple Liquids* (London: Academic)
[46] Ruppersberg H and Egger H 1975 *J. Chem. Phys.* **63** 4095
[47] Price D L 1990 *J. Non-Cryst. Solids* **117/118** 10
[48] Seifert-Lorenz K and Hafner J 2000 unpublished
[49] Iida T and Guthrie R I L 1988 *The Physical Properties of Liquid Metals* (Oxford: Oxford Science)
[50] Tegze M and Hafner J 1989 *Phys. Rev.* B **39** 8263
     Tegze M and Hafner J 1989 *Phys. Rev.* B **40** 9841
[51] Genser O and Hafner J 2001 to be published
[52] Jank W and Hafner J 1990 *Phys. Rev.* B **41** 1497
[53] Indlekofer G, Oelhafen P, Lapka R and Güntherodt H J 1988 *Z. Phys. Chem., NF* **157** 465
[54] Seifert K, Hafner J, Furthmüller J and Kresse G 1995 *J. Phys.: Condens. Matter* **7** 3883
[55] Kresse G, Furthmüller J and Hafner J 1994 *Phys. Rev.* B **50** 13 181